Doppler-Based Localization Under Hardware, Atmospheric and Orbital Impairments for Single LEO Satellite Systems

Citation for the original published paper (version of record):
Bezerra de Freitas Diniz, A., Eriksson, T., Gustavsson, U. et al (2026). Doppler-Based Localization Under Hardware, Atmospheric and Orbital Impairments for Single LEO Satellite Systems. IEEE Transactions on Aerospace and Electronic Systems, 62: 14870-14887.
http://dx.doi.org/10.1109/TAES.2026.3717291

(article starts on next page)

Doppler-Based Localization Under Hardware, Atmospheric, and Orbital Impairments for Single LEO Satellite Systems

ANDRÉ B. DE F. DINIZ, Student Member, IEEE
Chalmers University of Technology, Gothenburg, Sweden
Ericsson AB, Gothenburg, Sweden

THOMAS ERIKSSON, Member, IEEE
Chalmers University of Technology, Gothenburg, Sweden

ULF GUSTAVSSON
Ericsson AB, Gothenburg, Sweden

SHARIEF SALEH, Member, IEEE
HENK WYMEERSCH, Fellow, IEEE
Chalmers University of Technology, Gothenburg, Sweden

SEBASTIAN EULER
Ericsson AB, Kista, Sweden

In order to enable a wide range of applications anywhere and anytime, future communication systems are expected to employ low Earth orbit satellites to perform user verification. Single-satellite systems offer a cost-effective verification alternative, reducing implementation complexity and dependence on satellite constellations. This article develops a single-pass, single-satellite localization algorithm independent from global navigation satellite systems, supporting user verification and requiring only coarse coverage-region side information. The algorithm is based on the tracking of phase changes from received pilot signals originated from Doppler shifts, inherently related to the user's position. Our work addresses realistic channel and receiver conditions—encompassing carrier frequency offset, phase noise, and atmospheric propagation effects—while evaluating robustness against orbital perturbations, a combination that has not been jointly addressed in prior studies on Doppler-based localization. The proposed two-stage approach employs an extended Kalman filter for estimation of the referred phase shifts, followed by a weighted least squares solution. Algorithm performance is evaluated through simulations in terms of mean and 90th percentile distance error, together with the time to reach a 10-km error level, an accuracy benchmark discussed in verification studies by 3rd Generation Partnership Project (3GPP). Results demonstrate improved accuracy with respect to compatible Doppler-based baselines, with 90th percentile errors falling below the 10-km mark under the considered narrowband and line-of-sight conditions, suggesting that the method may support user verification. The time required to achieve such accuracy, particularly, may require a significant portion of the satellite's visibility window in strong phase noise conditions.

Received 23 January 2026; revised 24 May 2026; accepted 22 July 2026. Date of publication 28 July 2026; date of current version 18 August 2026.

DOI. No. 10.1109/TAES.2026.3717291

Refereeing of this contribution was handled by B. Jones.

This work was supported in part by the European Union, under ANTERRA through HORIZON-MSCA-2021-DN-01 under Grant 101072363 and in part by the Swedish Research Council under Grant 2022-06725.

Authors' addresses: André B. de F. Diniz is with the Chalmers University of Technology, 412 96 Gothenburg, Sweden, and also with Ericsson AB, 412 96 Gothenburg, Sweden, E-mail: (andredin@chalmers.se); Thomas Eriksson, Sharief Saleh, and Henk Wymeersch are with the Chalmers University of Technology, 412 96 Gothenburg, Sweden, E-mail: (thomase@chalmers.se; sharief@chalmers.se; henkw@chalmers.se); Ulf Gustavsson is with Ericsson AB, 412 96 Gothenburg, Sweden, E-mail: (ulf.gustavsson@ericsson.com); Sebastian Euler is with Ericsson AB, 164 40 Kista, Sweden, E-mail: (sebastian.euler@ericsson.com). (*Corresponding author: André B. de F. Diniz.*)

I. INTRODUCTION

With the ongoing rollout of 5G communication systems, global research efforts are moving toward upcoming 6G networks. One of the main goals of future communication generations is ubiquitous and ultra-reliable coverage, serving remote areas either on land or at sea. Moreover, 6G further aims to provide complementary services, such as sensing and localization [1]. The integration of these functionalities is expected to be a key enabler of a broad range of use cases, such as digital twins, environmental monitoring, and mapping for automated transportation [2].

For such purposes, the deployment of nonterrestrial networks (NTNs) will play a major role in 6G [1], [3], [4]. In recent years, low Earth orbit (LEO) satellites have gained attention due to lower cost, more favorable propagation, and shorter delays relative to higher orbits [5], [6], [7]. This has also raised interest in verification technologies operating independently from the well-established Global Navigational Satellite System (GNSS), which remains susceptible to significant vulnerabilities, including jamming, spoofing, and interference [8], [9], [10]. In this context, verification refers to assessing whether a claimed user equipment (UE) position is consistent with physical layer observations and system constraints, without necessarily determining the user's exact location. To ensure user privacy, prevent unauthorized access, and guarantee efficient resource allocation while complying with local regulations, it is necessary to develop GNSS-independent verification solutions, especially in areas poorly covered by ground networks.

In general, localization in LEO-based non-terrestrial networks (NTNs) may be performed with multiple-satellite or single-satellite systems. In the first case, accuracy in meter-scale can be achieved [8], [11], [12], [13], [14]. However, such solutions may require a relatively high number of satellites visible to the user, precise time synchronization between satellites and high complexity in terms of computations and onboard hardware. Single-satellite solutions, although less precise, offer a simpler alternative in terms of computational load, cost, and power consumption reduction while relaxing requirements on calibration and eliminating the necessity of strict intersatellite time synchronization [15], [16]. Accordingly, in this work,we focus on localization for single LEO satellite systems, as the increased simplicity makes them particularly attractive for practical and resource-constrained applications, including verification, as previously described. In this context, we exploit Doppler shifts for the localization task, since they may be measured with low-cost hardware and incorporated into mathematical formulations that relate the measurements to the UE's position [17].

In Doppler-based localization for single LEO satellite systems, several approaches have been developed under different system assumptions. The study in [18] applies Doppler shift measurements within a particle swarm optimization framework. A second-order cone programming approach is proposed in [16]. Another alternative is the direct application of Doppler measurements to the underlying orbit geometry. The work in [19] considers a rectilinear trajectory of the LEO satellite. In [20], virtual ground references are introduced to aid the localization. The principle developed in [21] utilizes a reference station in the vicinity of the UE's position.

Other studies focused on fusing Doppler shifts with other types of measurements. The approach in [15] explored Doppler shift and Doppler rate to propose a constrained unscented Kalman filter, where the states are the UE's position on Earth. A more recent study in [22] extends this concept, including Doppler acceleration. In [23], Doppler rate measurements are fused with measurements of the cosine angle between the satellite-UE line of sight (LOS) and the satellite's velocity.

While several studies have examined scenarios affected only by additive noise, others have incorporated broader disturbance sources. The work in [24] proposes a solution based on Doppler shifts, round trip time measurements and uncertainties in modeling the Earth's radius. The measurement errors are combined to yield a likelihood function that depends on the UE position. The study in [25] addresses constant frequency offset (CFO) over the Doppler shift measurements. In [26], the effect of CFO and clock bias is considered for the developed method, which is based on reconfigurable intelligent surfaces. Another important study was conducted in [27], where satellite state and oscillator errors are modeled. It is assumed, however, that the satellite has a global positioning system (GPS) receiver, so the developed solution is not GNSS-independent. Moreover, oscillator errors are not tracked and the simulated satellite position errors are in the scale of a few meters, which in GPS-free scenarios may be in the order of kilometers [28], [29].

Overall, existing localization approaches primarily rely on noisy Doppler shift measurements, diverging in whether additional impairments (hardware imperfections, atmospheric effects, and orbital dynamics) are explicitly modeled or neglected. Although a number of studies have modeled some of these perturbations, research that extensively considers their combined influence remains limited. This limitation provides the motivation of this article. We compare measurement and impairment assumptions from previous studies to those in our work in Table I.

A. Contribution

The main contribution of this work is a single satellite Doppler-based algorithm, independent from GNSS satellites and intersatellite synchronization, requiring only coarse coverage-region side information to resolve inherent ambiguities. The algorithm estimates the position of a static UE for single LEO satellite systems affected by CFO, phase noise (PN) and atmospheric and orbital impairments. In particular, by effectively addressing PN and an accurate model of the Earth's shape in our estimation framework, we show significant accuracy improvements with respect to methods that do not consider these aspects. We show, under the considered narrowband and LOS conditions, 90th percentile localization errors below a 10-km level referenced in 3rd Generation Partnership Project (3GPP) verification studies for NTNs [30], [31]. Results suggest that our method may provide position estimates supporting verification workflows, without itself implementing the full decision procedure. Robustness in relation to several system parameters and channel conditions is demonstrated through a comprehensive sensitivity analysis.

B. Article Outline

The rest of this article is organized as follows. In Section II, we model the relevant signal impairments and introduce the continuous-time and discrete-time system models describing satellite-to-ground (S2G) transmission and reception. In Section III, we propose an alternative signal representation and define the desired tracking parameter, which is directly related to the UE's position. We further develop and evaluate an extended Kalman filter (EKF) to track this parameter. Leveraging estimates of the desired parameter, we propose a weighted least squares (WLS) solution to estimate the CFO and the UE's position in Section IV, where a general overview of our localization algorithm is given. Its performance for several system and channel parameters is analyzed in terms of accuracy and convergence time in Section V, where we also perform a comparison to state-of-the-art methods. Finally, Section VI concludes this article.

II. SYSTEM MODEL

We describe the system model that characterizes the continuous-time received signals at the UE, considering that the received signals are affected by atmospheric, orbital, and hardware impairments. The atmospheric effects manifest as delays and the respective models used in this work are given in Appendix A. The orbital and hardware impairments

TABLE I
Comparison of Hardware and Impairment Assumptions for Doppler-Based Single-Satellite Localization

Assumption/reference	[18]	[16]	[19]	[20]	[15]	[22]	[23]	[21]	[24]	[25]	[26]	[27]	Our work
Single type measurements	✓	✓	✓	✓						✓	✓		✓
Atmospheric effects													✓
Perturbed satellite states										✓		✓	✓
Carrier frequency offset										✓	✓		✓
PN												✓	✓

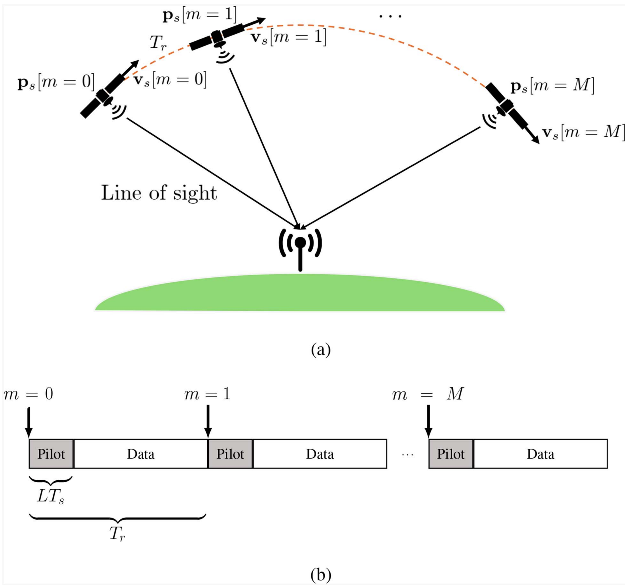

Fig. 1. Transmission–reception scheme and structure of the transmitted packets. Each of the $M+1$ pilot blocks is transmitted every T_r seconds over the duration of the satellite pass. The variables $\mathbf{p}_s[m]$ and $\mathbf{v}_s[m]$, respectively, denote the satellite's position and velocity at the transmission of the mth pilot block. (a) Satellite states (position and velocity) over slow-time epochs. (b) Packet structure containing pilot and data blocks.

TABLE II
System Simulation Parameters

Variable	**Value**	**Variable**	**Value**
e_c	0.001	a	$R_E + 700$ km
i	$50.12°$	Ω	$32°$
ω	$125.19°$	μ	$5.78°$
λ	$-123.3933°$	ϕ	$-48.8767°$
T_p	276 s	σ_B^2	10^{-17}
$\theta_{e,\min}$	$20°$	f_c	4 GHz
η	4 kHz	ε	3 km
f_s	25 MHz	T_r	1 s
G_{TX}	20 dBi	G_{RX}	0 dBi

are of higher relevance over the system model and so we present them in more detail in this section. To enable the estimation of parameters related to the UE's position, which is discussed in later sections, we present a discrete-time system model that also accounts for the aforementioned signal impairments.

We consider the transmission of signals from a single LEO satellite to a static ground terminal with known altitude (e.g., through the aid of an altimeter). Nonetheless, our proposed algorithm may be easily extended to include altitude as one of the estimated variables. Further, we consider continuous strong LOS conditions during the satellite's visibility window. The transmitted signals are packets containing pilot and data symbols. The packets have a duration T_r, and are transmitted at slow-time epochs $m = 0, \ldots, M$, where $M = \lceil T_p/T_r \rceil - 1$, and $T_p = MT_r$ denotes the duration of the satellite pass, as shown in Fig. 1(a).

The system is configured such that the satellite broadcasts its orbital parameters and the receiver is equipped with a wide-beam antenna that applies an angle-independent gain over the range of angles-of-arrival of the received signals. All received signals are sampled with a sampling rate f_s and the sampling period is denoted $T_s = 1/f_s$. As in [32] and [33], in each packet the data symbols are preceded by a pilot block of duration LT_s, where L denotes the number of pilot symbols. The packet structure is illustrated in Fig. 1(b). For the purposes of this study, we extract the necessary data for positioning solely from the pilot block.

We note that later derivations and simulations represent LOS-dominated downlink conditions in S-band (see Table II). From [34] and the simulated UE's position and elevation mask, attenuations due to rain and clouds, building entry, and scintillation may be neglected, so free-space path loss becomes the dominant factor in modeling the amplitude of the received signals.

A. CFO and PN models

We consider receiver systems considerably affected by CFO and PN. Receivers may also be affected by in-phase/quadrature (IQ) imbalance, generating an interfering signal image. Consequently, the phase of received signals may be significantly corrupted. In this study, we assume calibration with an image rejection ratio of at least 40 dB, implemented with strategies, such as that in [35]. Under the highest simulated signal-to-noise ratio (SNR) of 35 dB, the image term is thus 5 dB below the noise floor and its amplitude is 1% of the amplitude of the desired signal. This corresponds to the worst case phase contribution of approximately 0.01 rad, rapidly overcome by additive noise and PN. The following impairment models are generic abstractions, not tied to a specific receiver architecture.

As it will become clear in later sections, we investigate the phase of received signals. The CFO appears as a constant phase rotation per sample, which may degrade the performance of Doppler-based localization techniques.

The PN appears as random phase changes per sample, and may also degrade the performance. The phase may also be subject to several other hardware impairments. These, however, are generally almost constant phase shifts, and are dominated by CFO and PN. Thus, we model CFO and PN as the most important dynamics in the phase of the received signals. Moreover, we restrict our study to systems without significant intersymbol interference.

The continuous-time PN $\gamma(t)$ is modeled as a Wiener process [36]

$$\gamma(t) = \gamma(0) + \int_0^t g(\kappa)d\kappa \tag{1}$$

where $\gamma(0) \sim \mathcal{U}[0, 2\pi]$, and $g(\kappa)$ is a white Gaussian process with two-sided power spectral density σ^2. The discrete-time PN $\gamma_n = \gamma(nT_s)$ for a sampling period T_s is modeled as a discrete Wiener process, where [36], [37], [38]

$$\gamma_n = \gamma_{n-1} + g_n\sqrt{\sigma^2 T_s} = \gamma_{n-1} + u_n \tag{2}$$

with $g_n \sim \mathcal{N}(0, 1)$ and $u_n \sim \mathcal{N}(0, \sigma_u^2)$. Moreover, σ_u^2 denotes the PN innovation variance and $\gamma_0 \sim \mathcal{U}[0, 2\pi]$. In [38], low-to-moderate effects on the communication system can be seen for $\sigma_u^2 \leq 10^{-4}$, which we also adopt in this study. Hence, we consider strong PN for $\sigma_u^2 > 10^{-4}$.

B. Orbital Perturbations and Geometric Delays

Generally, the motion of any satellite can be described by six orbital parameters: eccentricity (e_c), semimajor axis (a), inclination (i), longitude of the ascending node (Ω), argument of periapsis (ω) and true anomaly (μ). To propagate the satellite's orbit based on these parameters, the Simplified General Perturbation 4 (SGP4) model is widely applied. Although accounting for many short-term and long-term effects, this model may yield relevant satellite position and velocity errors due to several factors acting over the satellite, such as gravitational forces, atmospheric drag, and solar radiation pressure. This makes information about satellite states, e.g., position and velocity, less precise over time, consequently reducing the accuracy of UE position estimates [14], [39].

Prior studies have reported that even with daily updates of the orbital parameters, the errors between predicted and actual satellite positions are mostly concentrated along the track of its orbit usually between 1–3 km, while velocity prediction errors are mostly concentrated in the radial direction, in a scale of 4–10 m/s [28], [29]. Moreover, without proper update of the orbital parameters, inaccuracies in the prediction of satellite states become even more severe [40], [41].

The aforementioned orbital perturbations, in particular, induce errors in the satellite's argument of latitude $\beta = \omega + \mu$. For a nearly circular orbit and an along-track position error of magnitude ε, we approximate this perturbed parameter with $\tilde{\beta} = \omega + \mu + \arcsin(\varepsilon/a)$ [28]. Based on [28] and [29], ε is modeled as having a uniformly random distribution within $[-3, 3]$ km.

The geometric delay experienced by a static ground receiver over time is given as a function of the satellite's position in the same reference frame as the UE. In the following, all positions and velocities are given in Earth-centered, Earth-fixed (ECEF) coordinates using the WGS84 model, which represents the shape of the Earth as an ellipsoid [42]. We define $\mathbf{p}_u^{(\lambda,\phi)}$ as the UE's position as a function of its longitude (λ) and latitude (ϕ), $\tilde{\mathbf{p}}_s(t)$ as the perturbed satellite's position propagated by the SGP4 model (due to $\tilde{\beta}$) at an arbitrary time t, and c as the speed of light. The geometric delay is given by

$$\tau^{(\lambda,\phi)}(t) = \frac{||\mathbf{p}_u^{(\lambda,\phi)} - \tilde{\mathbf{p}}_s(t)||}{c}. \tag{3}$$

C. Continuous-Time System Model

As previously discussed, $M + 1$ pilot blocks with L symbols each are transmitted and the blocks are spaced by T_r seconds. The continuous-time complex baseband pilot block with $n = 0, \ldots, L - 1$ at time t can thus be expressed as [43]

$$s(t) = \sum_{n=0}^{L-1} z_n h(t - nT_s) \tag{4}$$

where z_n denotes a pilot symbol with $|z_n| = 1$ and $h(t)$ a Nyquist pulse shape. As will be discussed in later sections, the unit-modulus pilot symbol assumption allows isolating the phase terms without introducing amplitude-dependent noise scaling, simplifying our derivations and further analysis. This is the case of constellations applying phase-shift keying [17], [44]. Nevertheless, the developed procedures can be performed by compensating for pilot symbols without unit absolute value, however at the cost of a modified noise contribution.

Following, the mth real-valued passband pilot block for $m = 0, \ldots, M$ is transmitted after mT_r seconds, and is given by

$$s_{m,\mathrm{RF}}(t) = 2\mathrm{Re}\{s(t - mT_r)e^{j2\pi f_c(t-mT_r)}\} \tag{5}$$

where $\mathrm{Re}\{\cdot\}$ represents the real part of a complex-valued number and f_c is the carrier frequency.

As it will be necessary in the following, we clarify the adoption of a narrowband model. Based on [45] and [46], Doppler stretching effects can be neglected if

$$WLT_s \ll \frac{c}{2|v_r|} \tag{6}$$

where W denotes the bandwidth of the transmitted signal and v_r denotes the satellite's radial velocity. For the longest simulated pilot block with $L = 6000$, a maximum bandwidth of 12.5 MHz, and based on the simulated parameters in Table II, the right-hand side of (6) is at least approximately 13 times higher than the product on the left-hand side. Thus, we adopt the narrowband model, consistent with previous practical work on real-world constellations [17], [47], [48]. Nevertheless, our proposed algorithm may be straightforwardly adapted to account for movement-induced time stretching in wideband signals.

As mentioned in Section II, we consider strong LOS conditions over the entire visibility window. Thus, the channel is modeled as having a single path that attenuates (through free space path loss), delays, and rotates the phase of the transmitted signals. The propagation delay, including geometric and atmospheric effects, is given by

$$\Delta(t) = \tau^{(\lambda,\phi)}(t) + \xi_{\mathrm{at}}(t) \tag{7}$$

with $\xi_{\mathrm{at}}(t)$ representing the atmospheric delay and $\tau^{(\lambda,\phi)}(t)$ as defined in (3). Accounting for attenuation and propagation delays, the mth received pilot-only passband signal may be written as

$$r_{m,\mathrm{RF}}(t) = 2D_m \mathrm{Re}\Big\{s(t - mT_r - \Delta(t)) \cdot e^{j2\pi f_c(t - mT_r - \Delta(t))}\Big\} + n(t) \tag{8}$$

where D_m denotes the amplitude of the received signal after the transmission of the mth block and $n(t)$ additive thermal noise.

We now incorporate the hardware impairments discussed in Section II-A. The receiver's local oscillator runs at a frequency $f_c + \eta$ (where η represents CFO) and introduces PN, denoted as $\gamma(t)$. As such, the signal $r_{m,\mathrm{RF}}(t)$ is downconverted by a factor $e^{-j2\pi(f_c+\eta)t}e^{j\gamma(t)}$ and lowpass filtered. The received complex baseband signal is shown to be given by (see Appendix B)

$$r_m(t) = D_m s(t - mT_r - \Delta(t))e^{j\alpha_m(t)} + n'(t) \tag{9}$$

where $n'(t)$ represents additive thermal noise. Moreover, the phase term is given by

$$\alpha_m(t) = -2\pi\left[f_c(mT_r + \Delta(t)) + t\eta\right] + \gamma(t). \tag{10}$$

For the following derivations, we introduce the notations $\Delta[\cdot]$, $\tau^{(\lambda,\phi)}[\cdot]$, and $\xi_{\mathrm{at}}[\cdot]$, respectively, denoting propagation, geometric, and atmospheric delays evaluated at the time given inside the square brackets.

D. Discrete-Time System Model

The received baseband signal $r_m(t)$, given in (9), is passed through a matched filter. After packet synchronization and symbol-timing recovery, the receiver obtains symbol-spaced samples corresponding to the instants $t = mT_r + nT_s + \Delta[mT_r + nT_s]$ for $n = 0, \ldots, L-1$. This can be done with techniques such as [49]. For a pulse shape with roll-off factor of 0.35, this method provides sampling timing errors with accuracy such that twice their standard deviation is approximately 4.5% and 0.35% of T_s for SNR values of 0 and 35 dB, respectively. This leads to distortion levels more than 10 dB below the respective noise floors, and so we neglect intersymbol interference [50]. The sampled received complex baseband signal is thus represented as

$$r_{m,n} = D_m z_n e^{j\alpha_{m,n}} + w_{m,n} \tag{11}$$

where $w_{m,n}$ corresponds to additive white Gaussian noise with variance σ_w^2.

In our study, given the application of short pilot blocks (in the order of microseconds, see Table II), the propagation delay variations within a single block are much smaller than T_s.[1] Although the intrablock delay variations cause negligible envelope distortion, their influence on phase is relevant. Phase rotations are induced by these delay variations that are magnified by f_c, i.e., Doppler shifts, while additional rotations arise from η. In deriving the phase term, we therefore refine our model by accounting for this effect and evaluate the propagation delays at $mT_r + nT_s$, yielding

$$\begin{aligned}\alpha_{m,n} = &-2\pi\left[f_c(mT_r + \Delta[mT_r + nT_s])\right.\\ &\left.+ (mT_r + nT_s + \Delta[mT_r + nT_s])\eta\right] + \gamma_{m,n}\end{aligned} \tag{12}$$

where $\gamma_{m,n}$ denotes the PN components at the aforementioned sampling instants.

III. PHASE TRACKING

We wish to estimate the UE's position based on variations in the phase of the received pilot signals. It is shown in (12) that the phase of the received signals contains variations directly related to UE's position through $\Delta[mT_r + nT_s]$, which in turn depends on $\tau^{(\lambda,\phi)}[mT_r + nT_s]$. Therefore, we investigate $\alpha_{m,n}$ in more detail. Due to the presence of PN and its recursive nature (typical of Wiener processes, see Section II-A), we propose an alternative phase representation to determine a desired trackable parameter, which is later leveraged to estimate the UE's position.

As it will become clear in later sections, we track a parameter of interest alongside PN. This requires the handling of a nonlinear measurement model and the recursive structure of the Wiener process, motivating the use of an EKF as the tracking framework. From the previously mentioned reformulated phase representation, in this section, we develop and evaluate the performance of the EKF to track the parameter of interest.

A. Reformulated Discrete-Time Phase Representation

As outlined earlier, it is of interest to extract information of $\alpha_{m,n}$, given its dependence on the UE's position. The terms in $\alpha_{m,n}$ are contained in the sampled received signal $r_{m,n}$, defined in (11). Its phase is not examined directly due to the phase contribution from the pilot symbols. To eliminate this contribution, we multiply $r_{m,n}$ by the conjugate of the pilot symbols z_n^*, giving

$$y_{m,n} = r_{m,n}z_n^* = D_m e^{j\alpha_{m,n}} + w'_{m,n}. \tag{13}$$

Since $|z_n| = 1$, as detailed in Section II-C, the mean and variance of the additive noise are preserved.

Applying a Taylor series expansion in n on (12), we rewrite the phase representation of the pilot signals as

$$\alpha_{m,n} = A_m + B_m n + \text{h.o.t.} + \gamma_{m,n}. \tag{14}$$

The higher order terms in (14) have very small values (see Appendix B) and so we neglect them. Thus, A_m and B_m are the most relevant terms, allowing for an approximation of

[1] In our simulations, the maximum propagation delay variation within a single block is approximately 8% of the value of T_s for $L = 6000$ and so envelope variations may be neglected, as a typical upper bound for such assumption is 10% of T_s (further details are discussed in Section II-C).

$\alpha_{m,n}$ as a first-degree polynomial in n. The coefficient A_m can be taken from (12) for $n = 0$, giving

$$A_m = -2\pi(f_c + \eta)(mT_r + \Delta[mT_r]). \tag{15}$$

The coefficient A_m is corrupted by $\gamma_{m,0} \sim \mathcal{U}[0, 2\pi]$, so relevant information embedded in it is lost. It becomes clear that the uncorrupted parameter B_m is the desired tracking parameter, as it contains information on the UE's position. From the proposed representation of (12) as a first-degree polynomial, the value B_m can be tracked from $\alpha_{m,n} - \alpha_{m,n-1}$ for any n. For simplicity, we consider the difference between the samples $n = 1$ and $n = 0$, so that

$$B_m = -2\pi\left[(f_c + \eta)(\Delta[mT_r + T_s] - \Delta[mT_r]) + T_s\eta\right]. \tag{16}$$

It is seen in (16) that B_m depends on $\Delta[mT_r + T_s]$, comprising the effect of geometric and atmospheric delays, as given in (7). To evaluate the geometric ones, defined in (3), it is necessary to determine the satellite's position in time. For this, we apply basic mechanics

$$\begin{aligned}\tilde{\mathbf{p}}_s(mT_r + nT_s) = \tilde{\mathbf{p}}_s(mT_r) &+ nT_s\tilde{\mathbf{v}}_s(mT_r)\\ &+ \frac{1}{2}(nT_s)^2\tilde{\mathbf{a}}_s(mT_r)\end{aligned} \tag{17}$$

where $\tilde{\mathbf{v}}_s(t)$ and $\tilde{\mathbf{a}}_s(t)$, respectively, denote the perturbed satellite's velocity and acceleration in ECEF coordinates.

B. EKF Formulation

A tracking method for the discussed parameter of interest is now developed. We note that the coefficient A_m only adds up to the uniformly random value of $\gamma_{m,0}$, so the phase term can be written as $\alpha_{m,n} = \gamma_{m,n} + B_m n$. From the recursive representation of Wiener processes, detailed in Section II-A, for a random increment $u_{m,n}$, we have

$$\begin{aligned}\alpha_{m,0} &= \gamma_{m,0}\\ \alpha_{m,1} &= \gamma_{m,1} + B_m\\ &= \gamma_{m,0} + u_{m,1} + B_m\\ \alpha_{m,2} &= \gamma_{m,2} + 2B_m\\ &= \gamma_{m,1} + 2B_m + u_{m,2}\\ &= \alpha_{m,1} + B_m + u_{m,2}\end{aligned}$$

and so on. By induction, the phase term has an alternative recursive representation $\alpha_{m,n} = \alpha_{m,n-1} + B_m + u_{m,n}$, which we use in the following. The recursive formulation of the phase terms provides a dynamical model for the defined states $\alpha_{m,n}$ and B_m. This serves as a basis for the development of an EKF to estimate B_m.

Before introducing the state-measurement representation, we estimate the amplitude based on the method of moments with [51]

$$\hat{D}_m = \sqrt{\frac{1}{L}\sum_{n=0}^{L-1}|y_{m,n}|^2 - \sigma_w^2} \tag{18}$$

where $y_{m,n}$ is given as in (13).

From the equivalent phase representation and measurements $y_{m,n}$, a nonlinear filtering problem can be formulated that involves $\alpha_{m,n}$ and B_m, which are given in (14). In general, nonlinear filtering problems may be written as [52]

$$\begin{aligned}\boldsymbol{\theta}_{n+1} &= \mathbf{f}(\boldsymbol{\theta}_n, \mathbf{v}_n)\\ \mathbf{g}_n &= \mathbf{h}(\boldsymbol{\theta}_n, \mathbf{w}_n)\end{aligned} \tag{19}$$

where $\mathbf{f}(\boldsymbol{\theta}_n, \mathbf{v}_n)$ denotes a function of $\boldsymbol{\theta}_n$ (the state vector at fast-time index n) and $\mathbf{v}_n$ (independent and white state noise). Furthermore, the measurements $\mathbf{g}_n$ are represented as a function of $\boldsymbol{\theta}_n$ and the independent and white measurement noise $\mathbf{w}_n$.

Based on the given equivalent phase representation in (14), we denote the state vector as $\boldsymbol{\theta}_n = [\hat{\alpha}_{m,n}, \hat{B}_{m,n}]^T$, where $\hat{\alpha}_{m,n}$ and $\hat{B}_{m,n}$, respectively, represent the tracked phase and B_m value at the fast-time index n. We model the state vector dynamics by

$$\boldsymbol{\theta}_{n+1} = \mathbf{A}\boldsymbol{\theta}_n + \mathbf{v}_n = \begin{bmatrix}1 & 1\\ 0 & 1\end{bmatrix}\boldsymbol{\theta}_n + \mathbf{v}_n. \tag{20}$$

The covariance matrix of the state noise is diagonal, containing the PN's innovation variance and a very small value σ_B^2 for tracking the constant B_m, namely, $\mathbf{Q}_\mathbf{v} = \mathrm{diag}([\sigma_u^2, \sigma_B^2])$.

Our proposed measurement model is given by

$$\begin{aligned}\mathbf{g}_n &= \begin{bmatrix}\mathrm{Re}\{y_{m,n}\}\\ \mathrm{Im}\{y_{m,n}\}\end{bmatrix}\\ &= D_m\begin{bmatrix}\cos(\alpha_{m,n})\\ \sin(\alpha_{m,n})\end{bmatrix} + \mathbf{w}_n\end{aligned} \tag{21}$$

where $\mathrm{Im}\{\cdot\}$ denotes the imaginary part of a complex-valued number. Since we take $\mathrm{Re}\{y_{m,n}\}$ and $\mathrm{Im}\{y_{m,n}\}$, the measurement noise covariance matrix is given by $\mathbf{Q}_\mathbf{w} = \frac{1}{2}\mathrm{diag}([\sigma_w^2, \sigma_w^2])$.

Before presenting the prediction and update equations, we calculate the Kalman gain by

$$\mathbf{K}_{m,n} = \mathbf{P}_{m,n}\mathbf{C}_{m,n}^T\left(\mathbf{C}_{m,n}\mathbf{P}_{m,n}\mathbf{C}_{m,n}^T + \mathbf{Q}_\mathbf{w}\right)^{-1} \tag{22}$$

where $\mathbf{P}_{m,n}$ represents the state error covariance matrix at index n, and $\mathbf{C}_{m,n}$ represents the measurement Jacobian matrix

$$\mathbf{C}_{m,n} = \hat{D}_m\begin{bmatrix}-\sin(\hat{\alpha}_{m,n}) & 0\\ \cos(\hat{\alpha}_{m,n}) & 0\end{bmatrix}. \tag{23}$$

Respectively, denoting $\hat{\boldsymbol{\theta}}_{n+1}$ and $\mathbf{P}_{n+1}$ as the predicted state and state error covariance matrix and based on (13.67–71) in [51], the prediction equations are

$$\begin{aligned}\hat{\boldsymbol{\theta}}_{n+1} &= \mathbf{A}\hat{\boldsymbol{\theta}}_n^+\\ \mathbf{P}_{m,n+1} &= \mathbf{A}\mathbf{P}_{m,n}^+\mathbf{A}^T + \mathbf{Q}_\mathbf{v}.\end{aligned} \tag{24}$$

The respective update equations are

$$\begin{aligned}\hat{\boldsymbol{\theta}}_{n+1}^+ &= \hat{\boldsymbol{\theta}}_{n+1} + \mathbf{K}_{m,n+1}\left(\mathbf{g}_{n+1} - \mathbf{c}(\hat{\boldsymbol{\theta}}_{n+1})\right)\\ \mathbf{P}_{m,n+1}^+ &= (\mathbf{I}_{2\times 2} - \mathbf{K}_{m,n+1}\mathbf{C}_{m,n+1})\mathbf{P}_{m,n+1}\end{aligned} \tag{25}$$

where $\hat{\boldsymbol{\theta}}_{n+1}^+$ denotes the updated a posteriori state estimate based on the predicted a priori state estimate $\hat{\boldsymbol{\theta}}_{n+1}$, and

$\mathbf{g}_{n+1} - \mathbf{c}(\hat{\boldsymbol{\theta}}_{n+1})$ contains the innovation, where

$$\mathbf{c}(\hat{\boldsymbol{\theta}}_n) = \hat{D}_m \begin{bmatrix} \cos(\hat{\alpha}_{m,n}) \\ \sin(\hat{\alpha}_{m,n}) \end{bmatrix}. \tag{26}$$

In addition, $\mathbf{P}^{+}_{m,n+1}$ represents the updated state error covariance matrix and $\mathbf{I}_{2\times 2}$ represents a 2×2 identity matrix.

In the following, we simulate the system using the parameters in Table II. We emphasize that the simulated parameters do not correspond to those of any particular constellation. Instead, they are representative values that may be assumed by any LEO satellite. This generalization is justified by the inherent ambiguity of Doppler shift profiles, making the underlying tracking problem mathematically generic across different orbits. The satellite orbit is propagated using the SGP4 model for 21 July 21 2025, from 11:00 to 13:00, with $\mathrm{TECV}(\lambda, \phi) = 10$ total electron content (TEC). The generated signals are subject to additive white Gaussian noise with equal power, so the SNR of the received signals is governed solely by the distance between the UE and the satellite. Further, we denote the Earth's mean radius by R_E, the minimum visibility elevation angle by $\theta_{e,\min}$, the minimum received SNR by $\mathrm{SNR}_{\min}$ (the SNR when the satellite is the furthest away from the UE), and G_{TX} and G_{RX} as the transmit and receive antenna gains, respectively.

To initialize the EKF, it is necessary to provide the prior mean of B_m and the corresponding error covariance values for each m. These prior statistics are obtained through offline Monte Carlo simulations over representative ranges of CFO, orbital perturbations, and orbital parameters of LEO satellites, and are used as a fixed, one-time initialization. For the orbital parameters, we simulated 5000 random and independent LEO satellite trajectories with a random UE position visible to the simulated satellite path. For this purpose, the respective orbital parameters are randomly drawn from uniform distributions within ranges of typical LEO satellite systems. More specifically, we take $e_c \in [0, 0.001]$, $a \in [R_E + 400\ \mathrm{km}, R_E + 2000\ \mathrm{km}]$, $i \in [0^\circ, 180^\circ]$, $\Omega \in [0^\circ, 360^\circ]$, $\omega \in [0^\circ, 360^\circ]$, and $\mu \in [0^\circ, 360^\circ]$. The CFO η and the satellite's along-track shift ε are uniformly randomized, respectively, within $[-6, 6]$ kHz and $[-3, 3]$ km. We then gather various candidate B_m values, so that the prior means are taken from the average for each m. The initial error variances for B_m are also drawn from such simulations. We initialize the phase with $\hat{\alpha}_{m,0} = \arctan(\mathrm{Im}\{y_{m,0}\}/\mathrm{Re}\{y_{m,0}\})$. Based on [51, Example (3.4)], the error variance respective to this estimate is taken as $\sigma_w^2/\hat{D}_m^2$.

In practical deployments, the receiver can be equipped with a precomputed lookup table of prior statistics categorized by orbital classes (e.g., nominal altitude and inclination ranges) and expected CFO bounds. No online simulation is required; rather, the table is fixed and satellite-agnostic within each orbital class (from broadcast two-line element sets), requiring no prepass information. Upon acquiring the satellite's orbital parameters, the receiver selects the best matching prior from the table, which needs to be updated only in substantially different orbital environments. A sensitivity analysis to different EKF initialization scenarios is given in Section V-H.

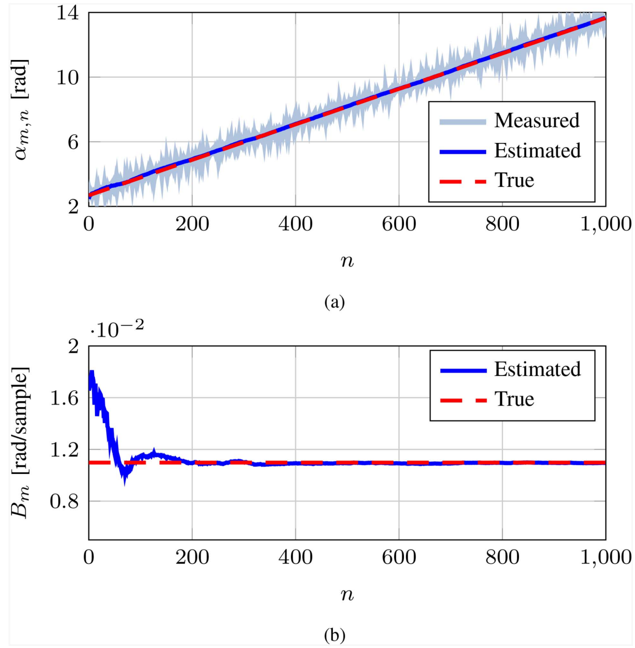

Fig. 2. Example of the proposed EKF's tracking performance ($\mathrm{SNR}_{\min} = 15$ dB and $\sigma_u^2 = 10^{-5}$) over fast-time indices n. (a) Example of tracked phase. (b) Example of tracked B_m value.

C. EKF Evaluation

We initially address performance of the proposed EKF, which is evaluated through simulations where we track $\alpha_{m,n}$ and B_m in an example case where $m = 20$. In this example, the measured, estimated, and true values of the unwrapped phase $\alpha_{m,n}$ and B_m are provided in Fig. 2 for $L = 1000$. It can be observed, for this case, that the proposed EKF is able to track the phase and converge toward the true value of B_m after few samples.

We conduct an analysis of the EKF's performance by verifying the empirical root-mean-square error (RMSE) in respect to B_m after $N_{\mathrm{MC}} = 10^4$ Monte Carlo simulations, for several values of $\mathrm{SNR}_{\min}$, σ_u^2, and L. To analyze the empirical root mean square error (RMSE), we provide the respective posterior Cramér–Rao lower bound (PCRB) as benchmarks for every L in different noise scenarios [52].

We start the analysis verifying the influence of $\mathrm{SNR}_{\min}$ over the performance of the proposed EKF in Fig. 3. For that purpose, we fix $\sigma_u^2 = 10^{-5}$ and vary $\mathrm{SNR}_{\min}$. It can be observed that for $\mathrm{SNR}_{\min} \geq 3$ dB, the EKF approaches the PCRB for all L. However, this is not the case for $\mathrm{SNR}_{\min} \leq 1$ dB. In such high-noise scenarios, we observe a considerable deviation from the PCRB for low values of L. To analyze the effect of PN, we fix $\mathrm{SNR}_{\min} = 15$ dB and vary the PN innovation variance σ_u^2 in Fig. 4. Even at relatively strong PN levels, corresponding to $\sigma_u^2 = 10^{-3}$, the RMSE approached the respective PCRBs.

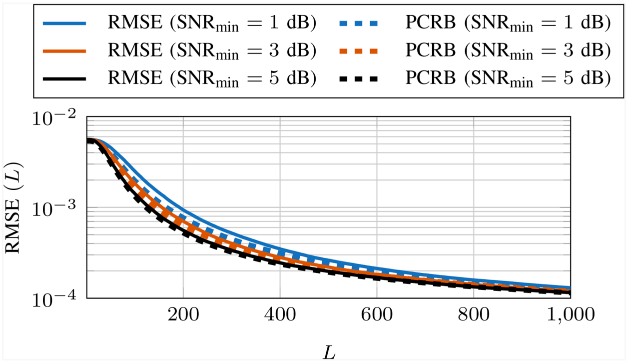

Fig. 3. Empirical RMSE of the proposed EKF for different SNR_{min} and L values ($\sigma_u^2 = 10^{-5}$). Deviations from the posterior Cramér-Rao lower bound (PCRB) are observed for the lowest SNR_{min} levels.

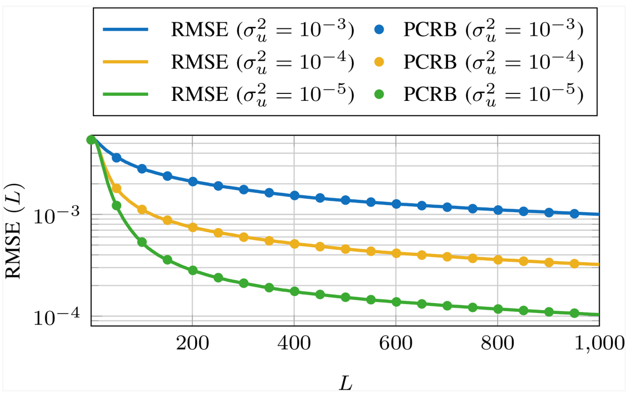

Fig. 4. Empirical RMSE of the proposed EKF for different σ_u^2 and L values ($\text{SNR}_{\text{min}} = 15$ dB). Despite strong PN levels, the EKF approximates the PCRB in all analyzed cases.

From the performance indicated in Figs. 3 and 4, we conclude that SNR_{min} has a significant influence over the EKF's performance, with the potential of relevant deviations from the PCRB. In regards to the PN's effect, the EKF has demonstrated to comply with the PCRB for a wide range of PN innovation variances.

IV. Doppler-Based UE Localization

Having acquired estimates of B_m, we propose a WLS solution to estimate the CFO η, the longitude λ, and the latitude ϕ. The problem is justified based on (3) and (16), which show a dependence of B_m on the aforementioned parameters. The CFO is an independent nuisance parameter that affects the accuracy of the estimation of the UE's geolocation, and so it is included in the problem. An example of true and estimated B_m values for the parameters in Table II is provided in Fig. 5.

A. Localization Problem Formulation

We introduce $\mathbf{b}_c^{(\eta,\lambda,\phi)}$ as the vector containing the B_m coefficients as a function of η, λ, and ϕ for $m = 0$ up to the current epoch m_c. From (3) and (16) and assuming perfect knowledge of the satellite states, the mth element of $\mathbf{b}_c^{(\eta,\lambda,\phi)}$

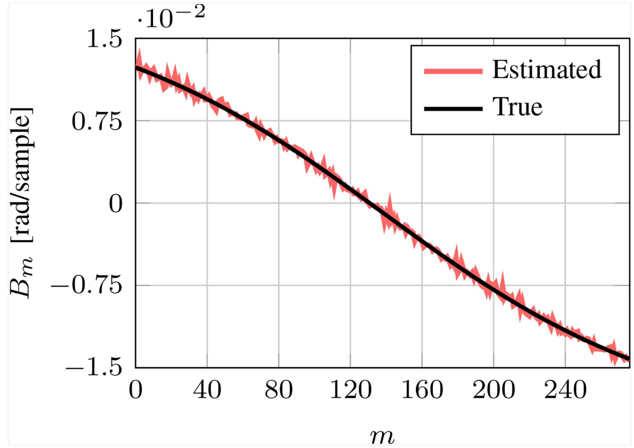

Fig. 5. Example of estimated and true B_m values over slow-time epochs m ($\text{SNR}_{\text{min}} = 15$ dB, $\sigma_u^2 = 10^{-4}$).

takes the form

$$b_m^{(\eta,\lambda,\phi)} = -2\pi \left[(f_c + \eta)(\tau^{(\lambda,\phi)}[mT_r + T_s] - \tau^{(\lambda,\phi)}[mT_r]) + T_s\eta \right]. \tag{27}$$

Note that (27) differs from (16) in that the formulation of $b_m^{(\eta,\lambda,\phi)}$ implies lack of complete knowledge of the propagation delays defined in (7), which in turn are embedded in B_m. Such mismatch comes from the absence of knowledge of atmospheric delays, which the receiver is not able to estimate with a simplified hardware. The compensation of atmospheric delays may be performed with dedicated hardware or with the aid of GNSS satellites, which we assume to be unavailable in this study [53], [54]. This represents an error source in the position estimation that only has a minor influence whatsoever, since the atmospheric delays are much smaller than the geometric ones (see Appendix A) [40].

We define $\hat{\mathbf{b}}_c$ as the vector containing all estimates $\hat{B}_m$ for $m = 0, \ldots, m_c$. Based on (27), the latest estimates of the desired parameters $(\hat{\eta}_c, \hat{\lambda}_c, \hat{\phi}_c)$ are found by solving the WLS equation

$$(\hat{\eta}_c, \hat{\lambda}_c, \hat{\phi}_c) = \underset{\eta,\lambda,\phi}{\arg\min} \left(\hat{\mathbf{b}}_c - \mathbf{b}_c^{(\eta,\lambda,\phi)}\right)^T \mathbf{G}_c^{-1} \times \left(\hat{\mathbf{b}}_c - \mathbf{b}_c^{(\eta,\lambda,\phi)}\right). \tag{28}$$

In this problem, $\mathbf{G}_c$ is a diagonal matrix containing the latest predicted state error covariances of $\hat{B}_m$, extracted from $\mathbf{P}_{m,L-1}^{+}$, given in (25), for $m = 0$ up to m_c.

Orbital perturbations, detailed in Section II-B, yield a constant uniformly random offset ε along the satellite's track with small velocity variations. To reduce errors in determining the UE's position, it is necessary to estimate ε. However, this may only be accurately performed in very low PN levels. To illustrate this concept, in Fig. 6, we show an example of the loss function based on (28) for an entire satellite pass as in Table II. We also assume perfect knowledge of η and λ, for unknown ε and ϕ. The variations in ϕ are converted into the distance to the UE's position $\mathbf{p}_u^{(\lambda,\phi)}$, where positive and negative values,

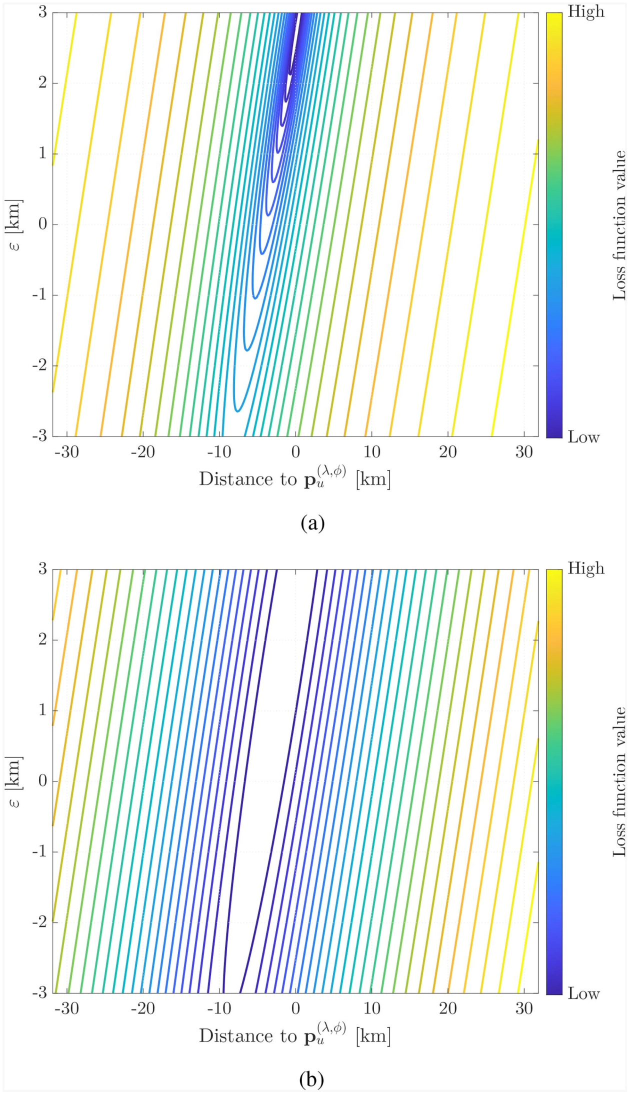

Fig. 6. Loss function for unknown ε and ϕ in different PN regimes. The loss function landscape becomes considerably flatter as PN levels increase, making the estimation of these parameters more challenging. In these examples, $\varepsilon = 3$ km. (a) Loss function for $\sigma_u^2 = 10^{-8}$. (b) Loss function for $\sigma_u^2 = 10^{-5}$.

respectively, denote coordinates to the north and to the south of the UE's true position. The loss function is given for $\text{SNR}_{\text{min}} = 15$ dB, $L = 2000$, and different PN innovation variance values ($\sigma_u^2 = 10^{-8}$ and $\sigma_u^2 = 10^{-5}$).

It is seen in Fig. 6(a) that a unique solution can be determined in very low PN scenarios. However, this does not hold for moderate PN levels. In Fig. 6(b), the loss function achieves low values for relatively large distances to the UE and different values of ε. As additional measurements are not available in the system, it is not possible to discriminate such candidate solutions, which may lie beyond accuracy benchmarks in [30] and [31]. In the absence of such measurements, we follow by performing the optimization without correcting the transmitted orbital parameters of the satellite. Through a sensitivity analysis conducted in later sections, we show that the performance of our proposed

Algorithm 1: UE Position Estimation Algorithm.

```
Inputs: m_c, r_{m_c,n}, T_s, T_r, σ_u^2, σ_w^2, σ_B^2, satellite's
 orbital parameters, geographical search space
Output: (η̂_c, λ̂_c, φ̂_c) Load pre-computed EKF
 prior statistics
Run EKF as in (18) and (22)-(26), get B̂_m
Store estimates B̂_m in b̂_c
if m_c < 2 then
    exit
else if m_c = 2 then
    Solve (28) by coarse-to-fine grid search, yield
    (η̂_c, λ̂_c, φ̂_c) [59]
else
    Solve (28) using the previous solution
    (η̂_{c−1}, λ̂_{c−1}, φ̂_{c−1}) as starting point, yield
    (η̂_c, λ̂_c, φ̂_c)
end if
```

algorithm is not significantly affected despite the presence of orbital perturbations.

We emphasize that the WLS solution stated in (28) inherently possesses two solutions: the true and a mirrored solution, located symmetrically with respect to the satellite's track [55]. To avoid reaching the mirrored solution, the proposed method operates under the assumption that the receiver has access to coarse coverage-region side information (e.g., through beam identification mechanisms [56], [57]) to identify the correct side of the satellite track. This allows the receiver to restrict the search space to a coverage region containing the correct side of the track. As such, in our simulations, we restrict the search space of the optimizer within a large area containing the true UE's position. The sensitivity of the proposed method to search region constraints is evaluated in Section V-G. In our simulations, based on Table II, we restrict the search space to be $\hat{\eta}_c \in [-6, 6]$ kHz, $\hat{\lambda}_c \in [-130^\circ, -100^\circ]$, and $\hat{\phi}_c \in [-90^\circ, -45^\circ]$. The proposed problem may be solved by several optimization techniques, such as the Nelder–Mead algorithm [58]. For that purpose, the previous solution $(\hat{\eta}_{c-1}, \hat{\lambda}_{c-1}, \hat{\phi}_{c-1})$ is used as a starting point. The overall UE position estimation algorithm is summarized in Algorithm 1.

V. NUMERICAL RESULTS AND ANALYSIS

We compare the performance of our proposed algorithm to state-of-the-art methods regarding the localization task and the estimation of the B_m coefficients in Section V-A. From Sections V-B to V-F, we study the impact of system and channel parameters (T_r, L, σ_u^2, SNR_{min}, and ε) over the accuracy of the estimated UE position. Sensitivity to geographical search space and EKF initialization is investigated in Sections V-G and V-H.

For the aforementioned evaluations, we establish 10 km as a verification accuracy benchmark (detailed in [30] and [31]) and define the mean distance error over the satellite's

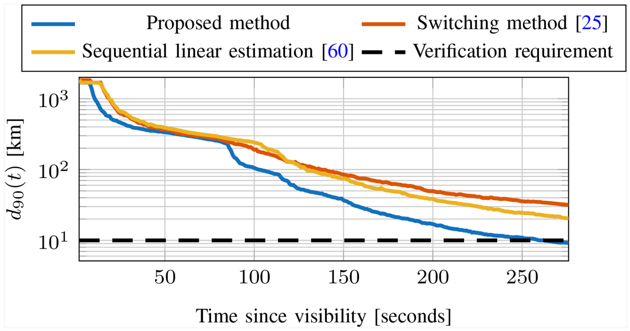

Fig. 7. 90th percentile distance error over time for different methods ($\mathrm{SNR}_{\min} = 15$ dB, $\sigma_u^2 = 2.5 \times 10^{-4}$, $T_r = 1$ s, $L = 6000$, and $\varepsilon = -3$ km). The error strongly increases without PN tracking and becomes even higher with inaccurate Earth models.

visibility window as

$$\overline{d}_e(t) = \frac{1}{N_S} \sum_{\ell=1}^{N_S} ||\mathbf{p}_u^{(\lambda,\phi)} - \hat{\mathbf{p}}_{u,\ell}^{(\lambda,\phi,t)}|| \tag{29}$$

where $\hat{\mathbf{p}}_{u,\ell}^{(\lambda,\phi,t)}$ denotes the ℓth estimated UE position for a given time t from N_S Monte Carlo simulations. The convergence time whenever the mean distance error is equal to or below 10 km, denoted as T_c, is also investigated. In addition to the mean error performance, we analyze the 90th distance error percentile over time $d_{90}(t)$ and denote the time to reach the 10 km accuracy benchmark for this metric as T_{90}. Due to the similarity in the convergence of the distance error curves over time, we show only $d_{90}(t)$. When analyzing system and channel parameters, T_c and T_{90} are also shown.

The parameters kept fixed across all realizations are detailed in the caption of the respective figure. The varied parameters, along with their corresponding ranges, are indicated in the figure legends in the $d_{90}(t)$ plots and the horizontal axis in convergence time plots. For each study, we conducted $N_S = 1000$ Monte Carlo simulations.

A. Comparison to State of the Art

In Fig. 7, we compare the performance of our developed method to techniques for estimation of B_m and Doppler-based localization. We perform the simulations under strong PN and orbital perturbations. The estimation method that we compare to was developed in [60], where a sequence of linear estimators is applied. Such technique has been shown to approach the Cramér–Rao lower bound for a wide range of SNR regimes. To compare the performance of this algorithm to ours, we apply the estimates of B_m from each method to the loss function in (28).

The method in [60] does not track PN, yielding very noisy estimates of B_m. Consequently, the presence of strong PN in such method heavily degrades the accuracy of the UE's position estimates, to the point that the verification requirement is not reached. Our proposed method, however, addresses PN through the structure of the EKF, based on the recursive nature of Wiener processes. This gives better estimates of B_m, achieving better accuracy in estimating the UE's localization and reaching the verification requirement.

Moreover, we assess the performance of the localization algorithm developed in [25], which addresses the effect of CFO. In the referred study, the presence of CFO is first detected by a switching procedure and then estimated. Hence, this technique is referred to as switching method. The CFO detection is governed by a sensitivity parameter N. The CFO-affected Doppler shift estimates and estimation error variances are taken from the technique in [60]. To ensure that the solutions from [25] remain within the bounds discussed in Section IV-A, we clip the result from each iteration to these limits. For execution of the algorithm, we choose $N = 2$ as a reference.

We observe that the error from the switching method is generally higher than applying the estimates of [60] into the loss function in (28). The main reason for such behavior is that all derivatives and error covariance matrices are given for a spherical Earth model. The resulting estimated coordinates, when applied to the more accurate WGS84 model (see Section II-B), yield relevant errors that remain above the verification requirement. In contrast, the WGS84 model is applied in our method, significantly reducing the errors regarding the UE's position estimates.

We emphasize that the results in Fig. 7 are intended as an illustrative compatibility analysis rather than a state-of-the-art ranking. While Table I lists several algorithms, our end-to-end comparison is limited to the aforementioned methods. Several Doppler-only techniques do not model additional impairments and so their performance is strongly hindered under the simulated conditions. Regarding other methods utilizing multiple observation types, a fair simulation-based comparison against single-type methods becomes difficult due to the distinct nature of the measurements. We thus acknowledge this limitation in our analysis. Further, we observe that reaching the verification threshold may require a significant portion of the visibility window, particularly in harsh conditions.

B. Effect of Period Between Transmissions (T_r)

We investigate the influence of the interval between pilot transmissions, with the results given in Fig. 8. It is shown, for the analyzed interpilot interval, that the proposed algorithm is able to produce UE location estimates with distance errors below the verification requirement for sufficiently short interpilot transmission periods. Longer intervals between pilot transmissions yield less estimates of B_m to be used in the optimization problem, reducing the localization accuracy and increasing the convergence time. This is more evident in Fig. 8, where convergence is not reached for $T_r = 20$ s when analyzing the 90th error percentile.

C. Effect of Number of Pilot Symbols (L)

Another relevant system design parameter is the number of pilot symbols. As seen in Figs. 3 and 4, for the same noise

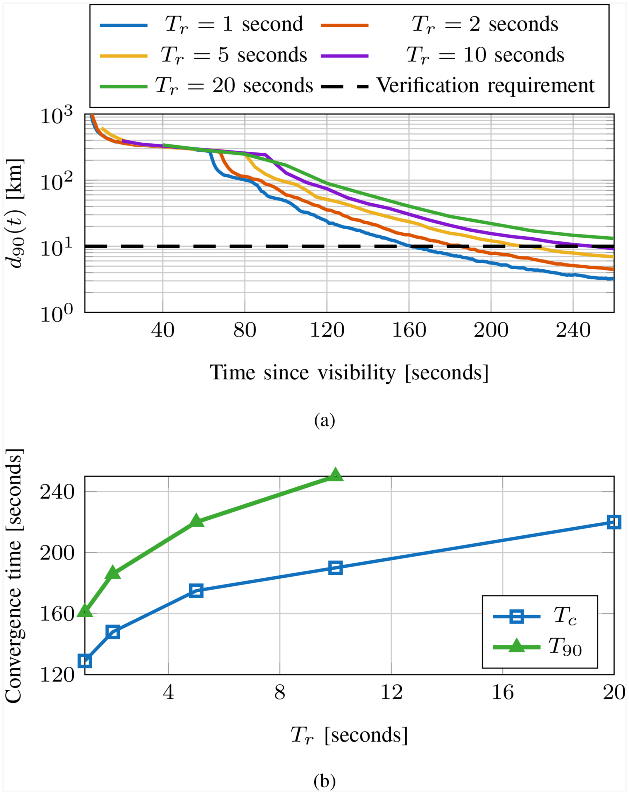

Fig. 8. 90th percentile distance error and convergence time for different T_r values and metrics ($\text{SNR}_{\text{min}} = 15$ dB, $\sigma_u^2 = 10^{-5}$, $L = 2000$, and no orbital perturbations). Shorter interpilot transmission intervals give more estimates of B_m for processing, improving accuracy. (a) 90th distance error percentile over time for different T_r values. (b) Mean and 90th percentile convergence times for varying T_r.

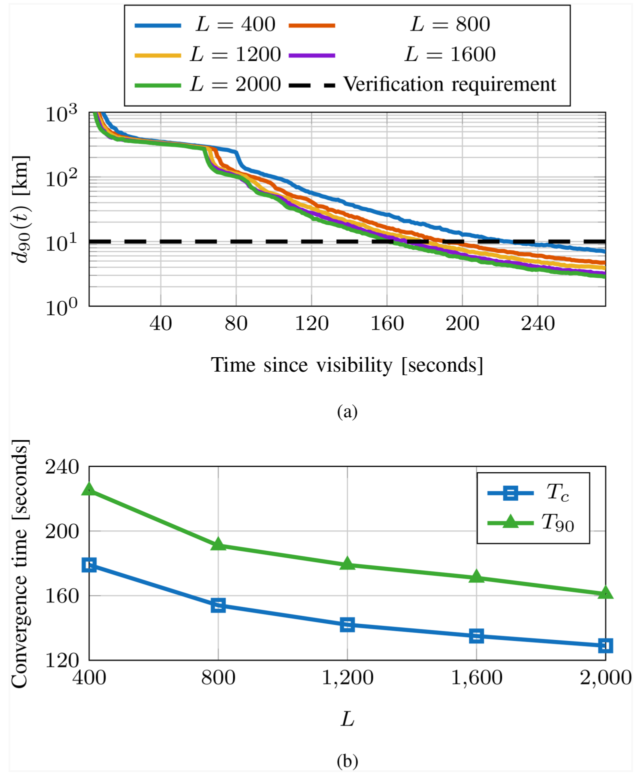

Fig. 9. 90th percentile distance error and convergence time for different L values and metrics ($\text{SNR}_{\text{min}} = 15$ dB, $\sigma_u^2 = 10^{-5}$, $T_r = 1$ second, and no orbital perturbations). Shorter pilot blocks have a higher RMSE, resulting in noisier estimates of B_m and reduced accuracy. (a) 90th distance error percentile over time for different L values. (b) Mean and 90th percentile convergence times for varying L.

level, the RMSE in the estimation of B_m is higher for shorter pilot blocks. In such cases, the influence of noise becomes more relevant and consequently the accuracy is expected to degrade. The algorithm's performance for different values of L is demonstrated in Fig. 9.

It is noted, as aforementioned, that applying fewer pilot symbols yield less accurate results, reflected upon positioning errors and convergence time. Conversely, having more pilot symbols provides more accurate UE position estimates and faster convergence, at the cost of a higher computational load and slower throughput. In comparison to the results in Fig. 8, similar performances can be achieved by changing either T_r or L, highlighting the tradeoffs involved in the system design.

D. Effect of PN Innovation Variance (σ_u^2)

Similar to the analysis in Section V-C, the PN innovation variance has the effect of increasing or decreasing the RMSE in the estimation of B_m, governing the positioning error. We show the influence of the PN innovation variance σ_u^2 in tenfold increases in Fig. 10.

We observe that for most analyzed PN innovation variances, our proposed algorithm is able to achieve convergence. Also, the convergence time is shown to be heavily dependent on σ_u^2. In the most severe case ($\sigma_u^2 = 10^{-3}$), however, the positioning error is considerably above the verification requirement. The developed EKF, although able to comply with the PCRB for tracking B_m in several PN conditions (see Fig. 4), provides estimates with increasingly larger errors as σ_u^2 grows. As a result, the coefficients $\hat{B}_m$ become more noisy, consequently degrading the performance of the proposed algorithm and highlighting the strong influence of PN. In such degrading conditions, the accuracy may be improved by transmitting longer pilot blocks, as the RMSE of $\hat{B}_m$ may be significantly reduced.

E. Effect of Minimum Received SNR (SNR_{min})

In analyzing the effect of additive noise, we note that it may not have a relevant influence over the final accuracy in low noise regimes, in which case PN and other impairments become the dominant perturbations over the received signals. In strong noise scenarios, additional phase distortions not captured by the presented signal models arise, introducing relevant inaccuracies.

From Fig. 11, it is noticeable that for $\text{SNR}_{\text{min}} \geq 5$ dB, there are no significant changes in performance, either in terms of positioning error or convergence time. As anticipated in Section III-C, strong additive noise regimes yield relevant model mismatches. For $\text{SNR}_{\text{min}} = -5$ dB, this effect becomes more pronounced. Despite the deviation from the respective PCRB as in Fig. 3, the RMSE

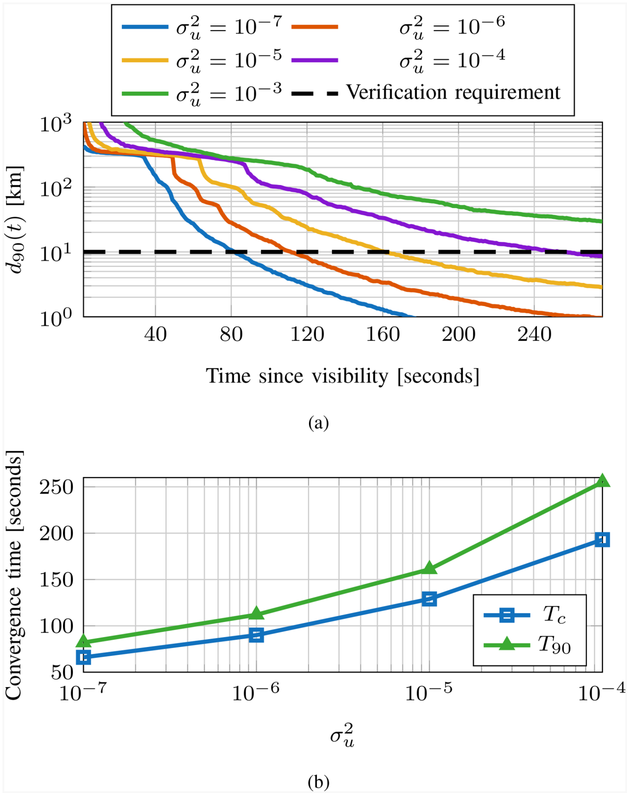

Fig. 10. 90th percentile distance error and convergence time for different σ_u^2 values and metrics ($\text{SNR}_{\min} = 15$ dB, $T_r = 1$ s, $L = 2000$, and no orbital perturbations). Stronger PN levels decrease accuracy and may require additional system resources to fulfill the verification requirement, such as longer pilot blocks. (a) 90th distance error percentile over time for different σ_u^2 values. (b) Mean and 90th percentile convergence times for varying σ_u^2.

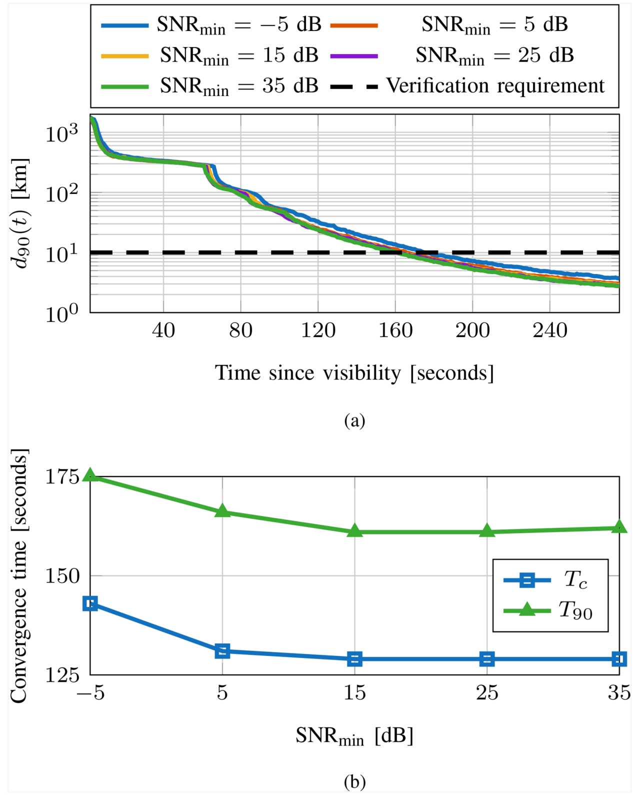

Fig. 11. 90th percentile distance error and convergence time for different $\text{SNR}_{\min}$ values and metrics ($\sigma_u^2 = 10^{-5}$, $T_r = 1$ s, $L = 2000$, and no orbital perturbations). The algorithm's performance is not significantly affected until strong additive noise becomes present. (a) 90th distance error percentile over time for different ε values. (b) Mean and 90th percentile convergence times for varying $SNR_{\min}$.

TABLE III
Sensitivity to Geographical Search Space Constraints

Geographical search space	**Final $d_{90}(t)$ (km)**	**T_{90} (seconds)**
$\hat{\lambda}_c \in [-130°, -100°]$, $\hat{\phi}_c \in [-90°, -45°]$ (correct)	2.86	161
$\hat{\lambda}_c \in [-130°, -80°]$, $\hat{\phi}_c \in [-90°, -10°]$ (loose)	2.85	163
$\hat{\lambda}_c \in [-160°, -130°]$, $\hat{\phi}_c \in [-45°, 0°]$ (mirror)	2015.78	N/A

remains low enough such that the UE's position may still be accurately estimated. These results illustrate that the proposed algorithm is able to reach the 10 km mark in the considered $\text{SNR}_{\min}$ range and assumed narrowband and LOS conditions.

F. Effect of Orbital Perturbations

Due to imprecise knowledge of the satellite states fed into the problem in (28), it is expected that orbital perturbations yield a bias over the UE's position estimate, as discussed in Section IV-A. Forward and backward satellite position shifts are, respectively, denoted with positive and negative values of ε.

As seen in Fig. 12, the analyzed orbital perturbations do not result in significant changes in convergence time. However, especially in the worst cases, i.e., $\varepsilon = \pm 3$ km, these disturbances make the final WLS solutions converge to a biased UE position estimate. This phenomenon is examined in more detail in Fig. 13, where the error in the UE's estimation accuracy has been increased by approximately 1.4 km in mean error and by approximately 2 km in 90th percentile error. Since ε is not usually higher than these values (see Section II-B), orbital perturbations do not pose a major challenge in reaching the verification requirement in our technique.

G. Geographical Search Space Sensitivity

To evaluate the dependence of the proposed algorithm on the region side information, we analyze the performance of the WLS stage under different geographical search space constraints. Three cases are compared: 1) a region containing the correct region identification (specified in Section IV-A); 2) a substantially enlarged search region on the correct side of the satellite track; 3) a search region constrained to the mirrored side of the satellite track. The simulations are performed for $\sigma_u^2 = 10^{-5}$, $T_r = 1$ s, $L = 2000$, $\text{SNR}_{\min} = 15$ dB, and no orbital perturbations. Table III summarizes the results.

The results show that our proposed method does not require highly precise side information, as performance

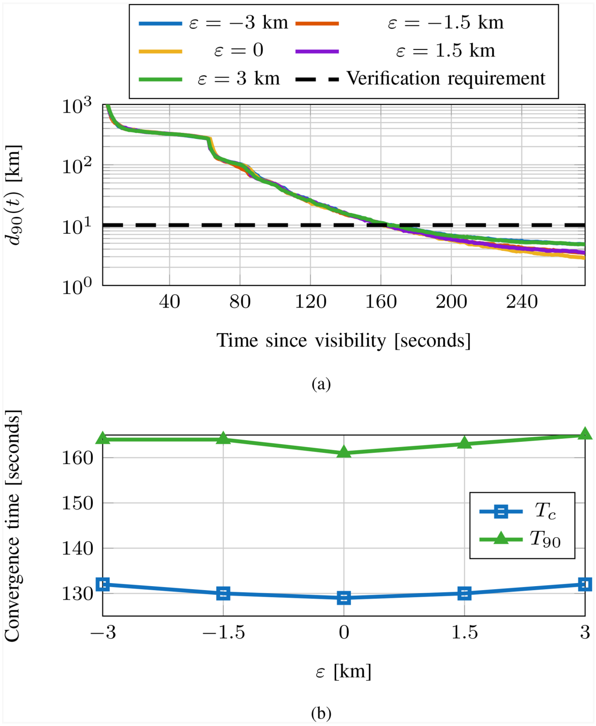

Fig. 12. 90th percentile distance error and convergence time for different ε values and metrics ($\text{SNR}_{\text{min}} = 15$ dB, $\sigma_u^2 = 10^{-5}$, $T_r = 1$ s, and $L = 2000$). Orbital perturbations do not significantly affect the convergence time and mainly translate into errors toward the end of the satellite pass. (a) 90th distance error percentile over time for different SNR_{min} values. (b) Mean and 90th percentile convergence times for varying $varepsilon$.

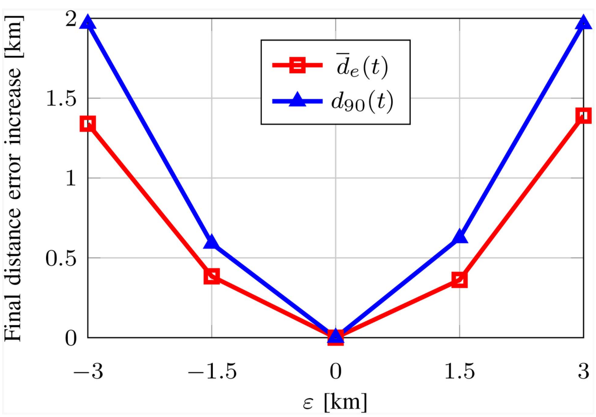

Fig. 13. Final mean distance error increase for different ε values and metrics.

does not significantly change even when with substantially larger geographical search space on the correct side of the satellite track. However, constraining the optimizer to the mirrored side of the trajectory leads to convergence toward symmetric solutions due to the ambiguity discussed in Section IV-A, leading to large errors. This demonstrates that coarse beam-assisted side information is sufficient, but necessary, to eliminate the referred ambiguities.

H. EKF Initialization Sensitivity

To evaluate sensitivity to the EKF prior statistics, we compare the performance of three different mismatch scenarios to the nominal initialization discussed in Section III-B while keeping the simulation parameters from Table II. The mismatch scenarios represent the following initialization while maintaining the other ones as in the nominal initialization: 1) high LEO satellite with $a \in [R_E + 1600, R_E + 2000]$ km; 2) polar orbit with $i \in [80°, 100°]$; and 3) overconfident prior with 20 times smaller initial covariance for all B_m. The simulations are conducted for a short pilot with $L = 400$ symbols, as prior information becomes more important with fewer iterations. Moreover, the simulations are performed for $\sigma_u^2 = 10^{-5}$, $T_r = 1$ s, $\text{SNR}_{\text{min}} = 15$ dB, and without orbital perturbations. The results are shown in Table IV.

TABLE IV
Sensitivity to EKF Initialization Mismatch

Mismatch scenario	**Final** $d_{90}(t)$ **(km)**	T_{90} **(seconds)**
High LEO	7.16	233
Polar orbit	6.97	228
Overconfident prior	8.34	255
Nominal initialization	6.98	225

We observe that for most mismatch scenarios, the performance is not significantly affected. In the high LEO case, Doppler shifts are usually lower due to reduced satellite speeds, biasing the EKF initialization. Moreover, the restriction in altitude creates local UE-satellite geometries such that a narrower range of Doppler shifts is observed, reducing the initial covariance (i.e., a more confident initialization). Such bias–covariance combination, however, only slightly reduces performance. In the polar orbit scenario, local UE-satellite geometries can still be generated that encompass a broad range of Doppler shifts, leading to a performance similar to the nominal case.

The overconfident prior case has the worst performance: even with nominal initial mean values, the substantially smaller initial covariances prevent the EKF from converging toward accurate estimates of B_m. Overall, the results show that the proposed EKF is not particularly sensitive to initial prior means; rather, it is more sensitive to overconfident initialization covariances. In this regard, for practical deployments, initialization may be performed with coarse orbit and UE location information.

VI. CONCLUSION

In this work, we presented a novel GNSS-independent and Doppler shift-based localization method for single-pass, single-LEO satellite systems jointly affected by several signal perturbations arising from atmospheric phenomena, orbital perturbations, and hardware defects. The proposed solution relies on tracking phase shifts in received pilot signals, which are inherently related to the UE's position. To track these phase shifts under the aforementioned signal impairments, an EKF was developed that complies with the PCRB for a wide range of channel and hardware conditions. After collecting estimates of the phase shifts, a WLS solution is proposed to estimate the UE's position and the CFO. The demonstrated performance shows that the proposed method may be used to support verification tasks in future NTNs.

Computer simulations have been performed to verify the performance of the algorithm under the various considered impairments. It has been shown that for most analyzed cases, the mean and 90th percentile distance errors remained below verification benchmarks referenced in 3GPP studies. Our proposed method has demonstrated considerably higher accuracy than the application of frequency estimation without PN tracking and simplified models for the Earth's shape. In addition, the time to achieve such convergence has been demonstrated to depend on different system design parameters, which can be adapted to balance computational load.

Although orbital perturbations are not compensated, robustness to this impairment has been demonstrated through a sensitivity analysis. In addition, it has been found that PN has a significant relevance over the performance of the developed localization method, strongly influencing the convergence time. Particularly, in the strongest analyzed PN condition ($\sigma_u^2 = 10^{-3}$), the algorithm fails to converge below the 10-km mark within the satellite visibility window. Such a result highlights the importance of tracking this impairment in realistic scenarios. Moreover, for relatively long interpilot transmission intervals, sufficient accuracy for verification was not reached in a significant amount of simulations.

Our study also shows that the method is not sensitive to the geographical search region size on the correct side of the satellite track, while an incorrect side assignment leads to large localization errors. This highlights the necessity of coarse but reliable coverage-region side information. Finally, we have shown that the proposed EKF is robust to prior mean mismatch, while overconfident initialization covariances represent the strongest performance degradation, suggesting that conservative covariance initialization is preferable in practical deployments.

APPENDIX A
ATMOSPHERIC EFFECTS

The atmospheric effects over the propagation of signals in S2G transmissions give rise to refractions, which mainly occur in the troposphere and the ionosphere, originating delays over the transmitted signal. The atmospheric delay at time t is represented as $\xi_{\text{at}}(t) = \xi_{\text{tr}}(t) + \xi_{\text{io}}(t)$, where $\xi_{\text{tr}}(t)$ and $\xi_{\text{io}}(t)$, respectively, denote the tropospheric and ionospheric delays. We introduce the utilized models for tropospheric and ionospheric delays in the following, with a brief worst case analysis for each of them.

1 Tropospheric Delays

We represent tropospheric delays with the Saastamoinen model [61], [62]. In this formulation, they are a function of temperature, humidity, pressure, and UE's latitude ϕ. Furthermore, the tropospheric delay at time t has contributions from dry and wet components, namely, $\xi_{\text{tr}}(t) = (\xi_{\text{tr,dry}}(t) + \xi_{\text{tr,wet}}(t))/c$, where c denotes the speed of light. The dry and wet components are, respectively

$$\xi_{\text{tr,dry}}(t) = \frac{0.0022768 \cdot P}{(1 - 0.00266 \cdot \cos 2\phi) \cos \theta_z(t)}$$
$$\xi_{\text{tr,wet}}(t) = \frac{0.002277 \cdot p_e (0.05 + 1255/T_K)}{\cos \theta_z(t)}.$$

Here, $P = 1013.25$ hPa denotes the local atmospheric pressure and $\theta_z(t)$ the zenith angle from the UE to the satellite. For a UE at sea level, the partial pressure of water vapor is

$$p_e = 6.108 \cdot h_r \cdot \exp\left(\frac{17.15 T_K - 4684}{T_K - 38.45}\right)$$

where h_r denotes the relative humidity (equal to 0.7 in this study). The local temperature in Kelvin scale is assumed to be $T_K = 288.16$ K in this work.

The dry component achieves its highest value for $\phi = 0$. Moreover, for $h_r = 1$ (maximum humidity) and $T_K = 313.16$ K (hot-day temperature), the wet components attain high values. For an elevation mask of 5° (corresponding to a maximum zenith angle of 85°), based on the aforementioned worst case values, the tropospheric delays for a typical satellite pass lie approximately within $[10^{-8}, 1.15 \times 10^{-7}]$ s, respectively, corresponding to additional path lengths of [3, 34.4] m.

2. Ionospheric Delays

Ionospheric delays, in contrast to tropospheric ones, are a function of the carrier frequency f_c. For carrier frequencies above 1 MHz, the ionospheric delay may be modeled by [63]

$$\xi_{\text{io}}(t) = \frac{40.3 \cdot 10^{16} \cdot \text{OF}(\theta_e(t)) \cdot \text{TECV}(\lambda, \phi)}{c f_c^2} \tag{30}$$

where $\text{OF}(\theta_e(t))$ denotes the obliquity factor for an elevation angle $\theta_e(t)$ from the UE to the satellite, and $\text{TECV}(\lambda, \phi)$ denotes the vertical total electron content in TEC units as a function of the user's position at a specific time (with λ denoting the UE's longitude), considered constant during the satellite pass. The values of $\text{TECV}(\lambda, \phi)$ for a given time may be consulted online. Further, the obliquity factor is calculated by

$$\text{OF}(\theta_e(t)) = \left[1 - \left(\frac{R_E \cos \theta_e(t)}{R_E + h_i}\right)^2\right]^{-1/2}$$

with $h_i = 350$ km as the mean ionospheric height and R_E being the mean radius of the Earth.

The temperature, humidity, pressure, mean ionospheric height, and total electron content related to the formulation of the described delay models are considered constant during the satellite pass. Hence, their variations are governed by the zenith and elevation angles involving satellite and UE. As we study the positioning of a static UE, the delay dynamics are solely dictated by the satellite dynamics. We note that based on the simulated system parameters, atmospheric attenuation losses may be neglected [64].

In [65], a maximum variation for $\mathrm{TECV}(\lambda, \phi)$ of 0.7 TEC units/s is reported. Assuming such an increasing variation of $\mathrm{TECV}(\lambda, \phi)$, based on the parameters in Table II, a maximum additional path length of approximately 11 m is generated. We note that due to their strong dependence on f_c, as in (30), ionospheric delays may have a stronger impact at lower carrier frequencies.

To evaluate the worst case effect of atmospheric delays over B_m, we simulate the path based on Table II with hot-day temperature and maximum humidity and variation of $\mathrm{TECV}(\lambda, \phi)$, starting from a high vertical total electron content of 40 TEC units. Based on (16), the atmospheric contribution is denoted by $B_{m,\mathrm{at}} = -2\pi[(f_c + \eta)(\xi_{\mathrm{at}}[mT_r + T_s] - \xi_{\mathrm{at}}[mT_r])]$ and the geometric one by $B_{m,\mathrm{ge}} = -2\pi[(f_c + \eta)(\tau^{(\lambda,\phi)}[mT_r + T_s] - \tau^{(\lambda,\phi)}[mT_r])]$. In our simulations, the maximum achieved value of the ratio $|B_{m,\mathrm{at}}/B_{m,\mathrm{ge}}|$ was found to be 4.68×10^{-3}, showing that atmospheric contributions are much smaller than geometric ones.

APPENDIX B
RECEIVED COMPLEX BASEBAND SIGNAL REPRESENTATION

Starting from $s_{m,\mathrm{RF}}(t)$, it can be shown that [43]

$$\begin{aligned} s_{m,\mathrm{RF}}(t) &= 2\mathrm{Re}\left\{s(t - mT_r)e^{j2\pi f_c(t-mT_r)}\right\} \\ &= s(t - mT_r)e^{j2\pi f_c(t-mT_r)} \\ &\quad + s^*(t - mT_r)e^{-j2\pi f_c(t-mT_r)}. \end{aligned}$$

Applying this representation to (8), it follows that the downconversion of the signal $r_{m,\mathrm{RF}}(t)$ by $e^{-j2\pi(f_c+\eta)t}e^{j\gamma(t)}$ gives the signal $r'_m(t)$, where

$$\begin{aligned} r'_m(t) = D_m &e^{j\gamma(t)}e^{-j2\pi f_c(mT_r+\Delta(t))}e^{-j2\pi t\eta} \\ &\cdot \left[s(t - mT_r - \Delta(t)) + s^*(t - mT_r - \Delta(t))\right. \\ &\left.\cdot\ e^{-j4\pi f_c t}\right]. \end{aligned}$$

The output of the downconverted signal is passed to a lowpass filter, which removes the factor originating from $s^*(t - mT_r - \Delta(t))$. Thus, the received complex baseband signal takes the form as in (9) and (10).

APPENDIX C
FIRST-ORDER PHASE REPRESENTATION

The phase terms $\alpha_{m,n}$ are given by (12). The propagation delays defined in (7), for the sampling instants given in Section II-D, are calculated accordingly by $\Delta[mT_r + nT_s] = \tau^{(\lambda,\phi)}[mT_r + nT_s] + \xi_{\mathrm{at}}[mT_r + nT_s]$. Since the geometric delays are much larger than the atmospheric ones, we focus on representing the former as a function of n [40]. Using (3) and (17), we have

$$\begin{aligned} \tau^{(\lambda,\phi)}[mT_r + nT_s] &= \frac{1}{c}\Big|\Big|\mathbf{p}_u^{(\lambda,\phi)} - \tilde{\mathbf{p}}_s(mT_r) \\ &- nT_s\tilde{\mathbf{v}}_s(mT_r) - \frac{1}{2}n^2T_s^2\tilde{\mathbf{a}}_s(mT_r)\Big|\Big| = \frac{1}{c}||\mathbf{q}||. \end{aligned} \tag{31}$$

The norm in (31) is calculated by

$$||\mathbf{q}|| = \sqrt{q_x^2 + q_y^2 + q_z^2} \tag{32}$$

where the x, y and z subscripts, respectively, denote the components of a vector in the x, y and z directions of the ECEF system.

The following derivations apply to any of these directions and so are written with the subscript k. For ease of notation, we omit the (λ, ϕ) superscript and the argument mT_r. Expanding (31), it follows that for any direction

$$\begin{aligned} q_k^2 = &(\tilde{p}_{s,k} - p_{u,k})^2 + 2T_s\tilde{v}_{s,k}(\tilde{p}_{s,k} - p_{u,k})n \\ &+ T_s^2(\tilde{v}_{s,k}^2 + \tilde{p}_{s,k}\tilde{a}_{s,k} - p_{u,k}\tilde{a}_{s,k})n^2 + T_s^3\tilde{v}_{s,k}\tilde{a}_{s,k}n^3 \\ &+ \frac{1}{4}T_s^4\tilde{a}_{s,k}^2n^4 \end{aligned} \tag{33}$$

with $p_{u,k}$ representing the user's position. Also, $\tilde{p}_{s,k}$, $\tilde{v}_{s,k}$, and $\tilde{a}_{s,k}$, respectively, denote the perturbed satellite's position, velocity, and acceleration.

In (33), we see that the geometric delays are a polynomial function of n. Due to the usually low values of T_s, we neglect the third-order and fourth-order terms. As such, we approximate (32) as

$$\begin{aligned} ||\mathbf{q}|| \approx &\Bigg[\sum_{k\in(x,y,z)}(\tilde{p}_{s,k} - p_{u,k})^2 \\ &+ 2T_sn\sum_{k\in(x,y,z)}\tilde{v}_{s,k}(\tilde{p}_{s,k} - p_{u,k}) \\ &+ T_s^2n^2\sum_{k\in(x,y,z)}(\tilde{v}_{s,k}^2 + \tilde{p}_{s,k}\tilde{a}_{s,k} - p_{u,k}\tilde{a}_{s,k})\Bigg]^{1/2} \\ = &\sqrt{K + an + bn^2}. \end{aligned} \tag{34}$$

It can be shown that a Taylor series expansion of (34) with respect to n gives

$$\begin{aligned} ||\mathbf{q}|| &\approx K^{1/2} + \frac{a}{2K^{1/2}}n + \frac{4bK - a^2}{8K^{3/2}}n^2 + O(n^3) \\ &= k_0 + k_1n + k_2n^2 + O(n^3). \end{aligned} \tag{35}$$

To evaluate the impact in excluding higher order terms, we establish a numerical bound on the residual relative to B_m, defined in (16), for the parameters in Table II. The worst case residual error occurs when the satellite is at zenith, so B_m attains its lowest absolute value while the Doppler rate (governing the second-order term k_2) reaches its maximum absolute value. In this case, $|k_2| = 2.84 \times 10^{-14}$ and the residual phase is determined by evaluating $2\pi(f_c + \eta)|k_2|L^2/c$ for the longest simulated pilot block, $L = 6000$. This results in a phase residual of approximately 8.56×10^{-5} rads. Thus, the residual has a minor impact over the proposed first-order representation. Moreover, with the additional components $nT_s\eta$ from (12), the phase $\alpha_{m,n}$ may be accurately approximated by a first-order polynomial in n as seen in (14).

ACKNOWLEDGMENT

Views and opinions expressed are however those of the author(s) only and do not necessarily reflect those of the European Union. Neither the European Union nor the granting authority can be held responsible for them. The authors would like to thank the National Academic Infrastructure for Supercomputing in Sweden (NAISS) for providing the resources.

REFERENCES

[1] H. Pennanen, T. Hänninen, O. Tervo, A. Tölli, and M. Latva-Aho, "6G: The intelligent network of everything," *IEEE Access*, vol. 13, pp. 1319–1421, 2025.

[2] ITU-R, "Framework and overall objectives of the future development of IMT for 2030 and beyond," International Telecommunication Union, Technical Specification (TS), M.2160-0, 2023.

[3] S. Prasad Tera, R. Chinthaginjala, G. Pau, and T. Hoon Kim, "Toward 6G: An overview of the next generation of intelligent network connectivity," *IEEE Access*, vol. 13, pp. 925–961, 2025.

[4] C. T. Nguyen et al., "Emerging technologies for 6G non-terrestrial-networks: From academia to industrial applications," *IEEE Open J. Commun. Soc.*, vol. 5, pp. 3852–3885, 2024.

[5] G. Araniti, A. Iera, S. Pizzi, and F. Rinaldi, "Toward 6G non-terrestrial networks," *IEEE Netw.*, vol. 36, no. 1, pp. 113–120, Jan./Feb. 2022.

[6] S. Saleh et al., "Integrated 6G TN and NTN localization: Challenges, opportunities, and advancements," *IEEE Commun. Standards Mag.*, vol. 9, no. 2, pp. 63–71, Jun. 2025.

[7] X. Luo, H.-H. Chen, and Q. Guo, "LEO/VLEO satellite communications in 6G and beyond networks–technologies, applications, and challenges," *IEEE Netw.*, vol. 38, no. 5, pp. 273–285, Sep. 2024.

[8] Q. Wei, X. Chen, Z. Ni, C. Jiang, Z. Huang, and S. Zhang, "Integrated Doppler positioning in a narrowband satellite system: Performance bound, parameter estimation, and receiver architecture," *IEEE Internet Things J.*, vol. 11, no. 6, pp. 10893–10910, Mar. 2024.

[9] W. Stock, R. T. Schwarz, C. A. Hofmann, and A. Knopp, "Survey on opportunistic PNT with signals from LEO communication satellites," *IEEE Commun. Surv. Tut.*, vol. 27, no. 1, pp. 77–107, Feb. 2025.

[10] C. Zhao, H. Qin, N. Wu, and D. Wang, "Analysis of baseline impact on differential Doppler positioning and performance improvement method for LEO opportunistic navigation," *IEEE Trans. Instrum. Meas.*, vol. 72, 2023, Art. no. 8501110.

[11] Z. M. Kassas et al., "Navigation with multi-constellation LEO satellite signals of opportunity: Starlink, OneWeb, Orbcomm, and iridium," in *Proc. IEEE/ION Position, Location, Navigation Symp.*, 2023, pp. 338–343.

[12] S. Li, Q. Zhang, B. Deng, B. Wu, and Y. Gao, "A fast and accurate LEO satellite-based direct position determination assisted by TDOA measurements," *China Commun.*, vol. 19, no. 1, pp. 92–103, 2022.

[13] Q. Wang, X. Chen, Q. Qi, M. Li, and W. Gerstacker, "Multiple-satellite cooperative information communication and location sensing in LEO satellite constellations," *IEEE Trans. Wireless Commun.*, vol. 24, no. 4, pp. 3346–3361, Apr. 2025.

[14] M. A. Hasan, M. H. Kabir, M. S. Islam, S. Han, and W. Shin, "A double-difference Doppler shift-based positioning framework with ephemeris error correction of LEO satellites," *IEEE Syst. J.*, vol. 18, no. 4, pp. 2157–2168, Dec. 2024.

[15] P. Ellis, D. V. Rheeden, and F. Dowla, "Use of Doppler and Doppler rate for RF geolocation using a single LEO satellite," *IEEE Access*, vol. 8, pp. 12907–12920 , 2020.

[16] C. Hao, X. Wan, X. Xu, and J. Yi, "Satellite-based emitter geolocation via second-order cone programming initialization," *IEEE Commun. Lett.*, vol. 28, no. 9, pp. 2141–2145, Sep. 2024.

[17] J. J. Khalife and Z. M. Kassas, "Receiver design for Doppler positioning with LEO satellites," in *Proc. IEEE Int. Conf. Acoust., Speech Signal Process.*, 2019, pp. 5506–5510.

[18] Y. Z. Bin, L. A. Nan, Z. Jiao, and L. Ming, "Constrained PSO algorithm for single satellite passive localization form Doppler shift measurements," in *Proc. 3rd Int. Conf. Adv. Comput. Theory Eng.*, 2010, pp. V2536–V2539.

[19] N. H. Nguyen and K. Doğançay, "Algebraic solution for stationary emitter geolocation by a LEO satellite using Doppler frequency measurements," in *Proc. IEEE Int. Conf. Acoust., Speech Signal Process.*, 2016, pp. 3341–3345.

[20] Y. D. Zhang, Y. Ding, K. Pham, D. Shen, and G. Chen, "Single-satellite location of ground electromagnetic interferer exploiting Doppler signatures," in *Proc. 58th Asilomar Conf. Signals, Syst., Comput.*, 2024, pp. 1109–1113.

[21] K.-M. Cheung, C. Lee, W. Jun, and G. Lightsey, "Single-satellite Doppler localization with law of cosines (LOC)," in *Proc. IEEE Aerosp. Conf.*, 2019, pp. 1–12.

[22] Y. Ding, C. Minkler, Y. D. Zhang, D. Shen, and K. Pham, "Single-satellite EMI geolocation via flexibly constrained UKF exploiting Doppler acceleration," *IEEE Signal Process. Lett.*, vol. 32, pp. 11–15, 2025.

[23] H. Li, M. Zhang, and F. Guo, "A novel single satellite passive location method based on one-dimensional cosine angle and Doppler rate of changing," in *Proc. IEEE Int. Conf. Signal Process., Commun. Comput.*, 2018, pp. 1–6.

[24] S. J. Nawaz, E. Cianca, T. Rossi, and M. De Sanctis, "Round trip time (RTT) and Doppler measurements for IoRT localization by a single-satellite," *IEEE Commun. Lett.*, vol. 28, no. 3, pp. 528–532, Mar. 2024.

[25] T. Amishima, "Switching-based FOA geolocation method with frequency offset by a single moving observation platform," *IEICE Trans. Commun.*, vol. E 108–B, no. 4, pp. 374–383, 2025.

[26] S. Saleh et al., "6G RIS-aided single-LEO localization with slow and fast Doppler effects," in *Proc. IEEE Globecom Workshops* (GC Workshops), 2024, pp. 1–7.

[27] P. B. Ellis and F. Dowla, "Single satellite emitter geolocation in the presence of oscillator and ephemeris errors," in *Proc. IEEE Aerosp. Conf.*, 2020, pp. 1–7.

[28] S. Hayek, J. Saroufim, and Z. M. Kassas, "Analysis and correction of LEO satellite propagation errors with application to navigation," in *Proc. ION GNSS, Int. Tech. Meeting Satell. Division Inst. Navigation*, 2024, pp. 1800–1811.

[29] N. Khairallah and Z. M. Kassas, "Ephemeris tracking and error propagation analysis of LEO satellites with application to opportunistic navigation," *IEEE Trans. Aerosp. Electron. Syst.*, vol. 60, no. 2, pp. 1242–1259, Apr. 2024.

[30] 3GPP, "Study on requirements and use cases for network verified UE location for non-terrestrial-networks (NTN) in NR," *3rd Gener. Partnership Project (3GPP)*, version 18.0.0, Tech. Rep. (TS) 38.882, 2022.

[31] 3GPP, "Release 18 description; summary of Rel-18 work items," *3rd Gener.n Partnership Project (3GPP)*, version 18.0.0, Tech. Rep. (TS) 21.918, 2025.

[32] Y. Handa, K. Tamura, H. Hayakawa, R. Tanaka, J. Cha, and C.-J. Ahn, "Maximum Doppler shift identification using decision feedback channel estimation," in *Proc. IEEE 29th Asia Pacific Conf. Commun.*, 2024, pp. 403–408.

[33] C. Gong, C. Ma, Y. Lv, and P. Zhu, "Fast high-precision Doppler frequency offset and rate joint estimation," in *Proc. 6th Int. Conf. Elect., Electron. Inf. Commun. Eng.*, 2025, pp. 741–744.

[34] 3GPP, "Study on New Radio (NR) to support non-terrestrial networks (Release 15)," 3rd Gener. Partnership Project (3GPP), version 15.4.0, Tech. Rep. (TR) 38.811, 2020.

[35] J. Meng et al., "I/Q linear phase imbalance estimation technique of the wideband zero-IF receiver," *Electronics*, vol. 9, no. 11, 2020, Art. no. 1787.

[36] S. Mandelli, M. Magarini, and A. Spalvieri, "Modeling the filtered and sampled continuous-time signal affected by Wiener phase noise," in *Proc. 19th Eur. Conf. Netw. Opt. Commun.*, 2014, pp. 173–178.

[37] A. Demir, A. Mehrotra, and J. Roychowdhury, "Phase noise in oscillators: A unifying theory and numerical methods for characterization," *IEEE Trans. Circuits Syst. I: Fundam. Theory Appl.*, vol. 47, no. 5, pp. 655–674, May 2000.

[38] B. Gävert, M. Coldrey, and T. Eriksson, "Phase noise estimation in OFDM systems," *IEEE Trans. Commun.*, vol. 73, no. 6, pp. 4349–4362 , Jun. 2025.

[39] J. Saroufim and Z. M. Kassas, "LEO ephemeris error modeling enabling long baseline correction for improved PNT," in *Proc. IEEE/ION Position, Location Navigation Symp.*, 2025, pp. 625–630.

[40] W. Stock, R. T. Schwarz, and A. Knopp, "Error source analysis for Doppler shift based opportunistic LEO-PNT with starlink signals," in *Proc. IEEE/ION Position Location Navigation Symp.*, 2025, pp. 774–781.

[41] C. Yang et al., "Doppler positioning of dynamic targets with unknown LEO satellite signals," *Electronics*, vol. 12, no. 11, 2023, Art. no. 2392.

[42] J. A. Slater and S. Malys, "WGS 84 — Past, present and future," in *Advances in Positioning and Reference Frames*, (International Association of Geodesy Symposia Series), vol. 118, Berlin, Heidelberg, Germany: Springer, 1998.

[43] D. Tse and P. Viswanath, *Fundamentals of Wireless Communication*. Cambridge, USA: Cambridge Univ. Press, 2005.

[44] S. Kozhaya, H. Kanj, and Z. M. Kassas, "Multi-constellation blind beacon estimation, Doppler tracking, and opportunistic positioning with OneWeb, starlink, iridium NEXT, and Orbcomm LEO satellites," in *Proc. IEEE/ION Position, Location Navigation Symp.*, 2023, pp. 1184–1195.

[45] M. Neinavaie, J. Khalife, and Z. M. Kassas, "Doppler stretch estimation with application to tracking globalstar satellite signals," in *Proc. MILCOM 2021-2021 IEEE Mil. Commun. Conf.*, 2021, pp. 647–651.

[46] T. Zhao and T. Huang, "Cramer-Rao lower bounds for the joint delay-Doppler estimation of an extended target," *IEEE Trans. Signal Process.*, vol. 64, no. 6, pp. 1562–1573, Mar. 2016.

[47] Y. Liu, Y. Xu, M. Lei, M. Gao, Z. Fang, and Y. Mao, "A joint high-precision frequency and code phase estimation algorithm for iridium NEXT satellites' signals of opportunity," *IEEE Trans. Instrum. Meas.*, vol. 74, 2025, Art. no. 8508217.

[48] J. Khalife, M. Neinavaie, and Z. M. Kassas, "The first carrier phase tracking and positioning results with starlink LEO satellite signals," *IEEE Trans. Aerosp. Electron. Syst.*, vol. 58, no. 2, pp. 1487–1491, Apr. 2022.

[49] D.-Z. Liu and C.-H. Wei, "Asynchronous symbol timing recovery with adaptive interpolation filter for high data-rate digital mobile radio," in *Proc. IEEE Int. Symp. Circuits Syst.*, 2000, pp. 85–88.

[50] J. G. Proakis and M. Salehi, *Digital Communications*, 5th ed. New York, NY, USA: McGraw-Hill, 2008.

[51] S. M. Kay, *Fundamentals of Statistical Signal Processing: Estimation Theory*. Upper Saddle River, NJ, USA: Prentice-Hall, 1993.

[52] P. Tichavsky, C. Muravchik, and A. Nehorai, "Posterior Cramér-Rao bounds for discrete-time nonlinear filtering," *IEEE Trans. Signal Process.*, vol. 46, no. 5, pp. 1386–1396, May 1998.

[53] L. Bian, "Study on ionospheric delay correction in GPS signal," in *Proc. IEEE 11th Int. Conf. Electron. Meas. Instrum.*, 2013, pp. 79–83.

[54] C. Shi, Y. Zhang, and Z. Li, "Revisiting Doppler positioning performance with LEO satellites," *GPS Solutions*, vol. 27, 2023, Art. no. 126.

[55] N. Levanon, "Quick position determination using 1 or 2 LEO satellites," *IEEE Trans. Aerosp. Electron. Syst.*, vol. 34, no. 3, pp. 736–754, Jul. 1998.

[56] M. Elsanhoury, J. Koljonen, F. S. Prol, M. S. Elmusrati, and H. Kuusniemi, "Massive MIMO beam ID-based positioning method with low Earth orbit satellite mega constellations," *IEEE J. Radio Freq. Identif.*, vol. 9, pp. 619–634, 2025.

[57] 3GPP, "Solutions for NR to support non-terrestrial networks (NTN)," *3rd Gener. Partnership Project (3GPP)*, version 16.2.0, Tech. Rep. (TR) 38.821, 2023.

[58] J. Lagarias, J. Reeds, M. Wright, and P. Wright, "Convergence properties of the Nelder-Mead simplex method in low dimensions," *SIAM J. Optim.*, vol. 9, no. 1, pp. 112–147, 1998.

[59] Z. Xu et al., "Doppler positioning with LEO mega-constellation: Equation properties and improved algorithm," *Remote Sens.*, vol. 16, 2024, Art. no. 2958.

[60] A. B. de Freitas Diniz, T. Eriksson, and U. Gustavsson, "Doppler shift estimation for satellite communications using linear estimators," in *Proc. IEEE 25th Int. Workshop Signal Process. Adv. Wirel. Commun.*, 2024, pp. 686–690.

[61] J. Saastamoinen, "Atmospheric correction for the troposphere and stratosphere in radio ranging satellites," *Amer. Geophys. Union*, 1972, pp. 247–251.

[62] Y.-X. Yang and S.-S. Jan, "Error correction analysis and enhanced algorithm for standalone Doppler-based positioning using iridium-next and Orbcomm constellations," in *Proc. IEEE/ION Position, Location Navigation Symp.*, 2025, pp. 678–686.

[63] J. Khalife and Z. Kassas, "Assessment of differential carrier phase measurements from Orbcomm LEO satellite signals for opportunistic navigation," in *Proc. 32nd Int. Tech. Meeting Satell. Division Inst. Navigation*, 2019, pp. 4053–4063.

[64] ITU-R, "Propagation data and prediction methods required for the design of Earth-space telecommunication systems," International Telecommunication Union, Technical Specification (TS), P.618-14, 2023.

[65] ITU-R, "Recommendation ITU-R P.531-15: ionospheric propagation data and prediction methods required for the design of satellite networks and systems," International Telecommunication Union, Recommendation ITU-R P.531-15, 2023.

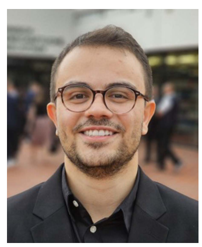

André B. de F. Diniz (Student Member, IEEE) received the B.Sc. degree in electrical engineering from the Federal University of Rio Grande do Norte, Natal, Brazil, in 2020, and the M.Sc. degree with distinction in communications and multimedia engineering from Friedrich-Alexander-Universität Erlangen-Nürnberg, Erlangen, Germany, in 2023. He is currently working toward the joint Ph.D. degree (a Marie Skłodowska-Curie Actions industrial Ph.D.) with Ericsson AB, Sweden, and Chalmers University of Technology, Gothenburg, Sweden.

From 2018 to 2023, he was a Student Research Assistant with Fraunhofer FHR, Wachtberg, Germany, and Fraunhofer IIS, Erlangen, Bang & Olufsen, Struer, Denmark, and the Brazilian National Telecommunications Agency, Brasília, Brazil. His research interests include signal processing for 6G nonterrestrial networks, estimation theory, and adaptive filtering.

Thomas Eriksson (Member, IEEE) received the Ph.D. degree in information theory from the Chalmers University of Technology, Gothenburg, Sweden, in 1996.

Between 1997 and 1998, he was with AT&T Labs—Research, Murray Hill, NJ, USA. Between 1998 and 1999, he was with Ericsson Radio Systems AB, Kista, Sweden. From 2003 to 2004, he was a Guest Professor with Yonsei University, Seoul, South Korea. Since 1999, he has been with Chalmers University, where he is currently a Professor of communication systems. He is a Researcher with the Chalmers University of Technology. He has authored or coauthored more than 300 journal and conference papers, and holds 20 patents. His research interests include communication, radar signal processing, and modeling and compensation of nonideal hardware components (e.g. amplifiers, oscillators, ADC/DAC and modulators).

Ulf Gustavsson received the M.Sc. degree in electrical engineering from Örebro University, Örebro, Sweden, in 2006, and the Ph.D. degree in signal processing and microwave electronics from the Chalmers University of Technology, Gothenburg, Sweden, in 2011.

His background ranges from power amplifier design to radio signal processing. He is currently a Senior Specialist with Ericsson Research. He is also the Lead Scientist from Ericsson Research with the Marie Skodowska-Curie European Industrial Doctorate Innovative Training Net-works, SILIKA, MyWave and ANTERRA. His research interests include novel radio signal processing techniques for hardware impairment mitigation and behavioral modeling of radio hardware for future advanced antenna systems and communication engineering.

Sharief Saleh (Member, IEEE) received the B.Sc. and M.Sc. degrees in electrical engineering from Qatar University, Doha, Qatar, in 2016 and 2018, respectively, and the Ph.D. degree in electrical engineering from Queen's University, Kingston, ON, Canada, in 2023.

He is currently a Marie Skłodowska-Curie Actions Postdoctoral Fellow with the Chalmers University of Technology, Gothenburg, Sweden. His current research interests include 5G and 6G positioning in terrestrial and nonterrestrial networks, channel modeling and estimation, and sensor fusion.

Henk Wymeersch (Fellow, IEEE) received the Ph.D. degree in electrical engineering/applied sciences from Ghent University, Ghent, Belgium, in 2005.

He is currently a Professor of communication systems with the Department of Electrical Engineering, Chalmers University of Technology, Gothenburg, Sweden, and a Distinguished Visiting Professor with Tsinghua University, Beijing, China. From 2005 to 2009, he was a Postdoctoral Researcher with the Laboratory for Information and Decision Systems, Massachusetts Institute of Technology, Cambridge, MA, USA. His research focuses on the convergence of communication and sensing, in a 5G and beyond 5G context.

Dr. Wymeersch was an Associate Editor for IEEE COMMUNICATION LETTERS, IEEE TRANSACTIONS ON WIRELESS COMMUNICATIONS, and IEEE TRANSACTIONS ON COMMUNICATIONS,and is currently Senior Member of the IEEE Signal Processing Magazine Editorial Board. From 2019 to 2021, he was an IEEE Distinguished Lecturer with the Vehicular Technology Society.

Sebastian Euler received the Ph.D. degree in particle physics from RWTH Aachen University, Aachen, Germany, in 2014.

In 2016, he joined Ericsson Research, Stockholm, Sweden. He is currently a Master Researcher with Ericsson Research, where he drives the standardization of NTN in 3GPP. He is also a delegate to the ITU-R, engaging in the standardization of the satellite component of IMT. He has contributed to academic articles and to the book "*5G and Beyond: Fundamentals and Standards.*"

Dr. Euler was the recipient of the IEEE Communications Society Fred W. Ellersick Prize.